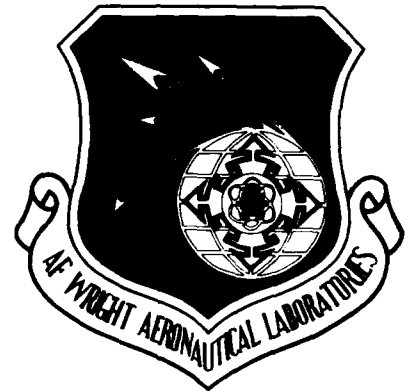


DTIC FILE COPY

2

AFWAL-TR-87-3051

AD-A201 075



IMPLICIT ALGORITHM FOR NUMERICAL SOLUTION OF THE LAMINAR
INCOMPRESSIBLE TWO-DIMENSIONAL NAVIER-STOKES EQUATIONS

D. P. Rizzetta

Aerodynamics and Airframe Branch
Aeromechanics Division

May 1988

Final Report for Period November 1985 - May 1987

Approved for public release; distribution unlimited.

DTIC
ELECTE
DEC 07 1988
S E D

FLIGHT DYNAMICS LABORATORY
AIR FORCE AERONAUTICAL LABORATORIES
AIR FORCE SYSTEMS COMMAND
WRIGHT-PATTERSON AFB, OHIO 45433-6553

88 12

NOTICE

When Government drawings, specifications, or other data are used for any purpose other than in connection with a definitely Government-related procurement, the United States Government incurs no responsibility or any obligation whatsoever. The fact that the Government may have formulated or in any way supplied the said drawings, specifications, or other data, is not to be regarded by implication, or otherwise in any manner construed, as licensing the holder, or any other person or corporation; or as conveying any rights or permission to manufacture, use, or sell any patented invention that may in any way be related thereto.


This report has been reviewed by the Office of Public Affairs (ASD/PA) and is releasable to the National Technical Information Service (NTIS). At NTIS, it will be available to the general public, including foreign nations.

This technical report has been reviewed and is approved for publication.


JOSEPH J.S. SHANG
Technical Manager


ROBERT R. JEFFRIES, Acting Chief
Aerodynamics & Airframe Branch

FOR THE COMMANDER


ROBERT C. HELT, COLONEL, USAF
Chief, Aeromechanics Division
Flight Dynamics Laboratory

If your address has changed, if you wish to be removed from our mailing list, or if the addressee is no longer employed by your organization please notify AFWAL/FIMM, W-PAFB, OH 45433-6553 to help us maintain a current mailing list.

Copies of this report should not be returned unless is required by security considerations, contractual obligations, or notice on a specific document.

REPORT DOCUMENTATION PAGE			Form Approved OMB No. 0704-0188	
1a. REPORT SECURITY CLASSIFICATION Unclassified			1b. RESTRICTIVE MARKINGS	
2a. SECURITY CLASSIFICATION AUTHORITY			3. DISTRIBUTION / AVAILABILITY OF REPORT Approved for public release; distribution unlimited	
2b. DECLASSIFICATION / DOWNGRADING SCHEDULE				
4. PERFORMING ORGANIZATION REPORT NUMBER(S) AFWAL-TR-87-3051			5. MONITORING ORGANIZATION REPORT NUMBER(S)	
6a. NAME OF PERFORMING ORGANIZATION Flight Dynamics Laboratory AFWAL, AFSC		6b. OFFICE SYMBOL (if applicable) AFWAL/FIMM		7a. NAME OF MONITORING ORGANIZATION
6c. ADDRESS (City, State, and ZIP Code) Wright-Patterson Air Force Base, Ohio 45433-6553			7b. ADDRESS (City, State, and ZIP Code)	
8a. NAME OF FUNDING / SPONSORING ORGANIZATION		8b. OFFICE SYMBOL (if applicable)		9. PROCUREMENT INSTRUMENT IDENTIFICATION NUMBER
8c. ADDRESS (City, State, and ZIP Code)			10. SOURCE OF FUNDING NUMBERS	
			PROGRAM ELEMENT NO. 61102F	PROJECT NO. 2307
			TASK NO. N6	WORK UNIT ACCESSION NO. 2307N611
11. TITLE (Include Security Classification) IMPLICIT ALGORITHM FOR NUMERICAL SOLUTION OF THE LAMINAR INCOMPRESSIBLE TWO-DIMENSIONAL NAVIER-STOKES EQUATIONS				
12. PERSONAL AUTHOR(S) Rizzetta, D. P.				
13a. TYPE OF REPORT Final		13b. TIME COVERED FROM Nov 85 TO May 87		14. DATE OF REPORT (Year, Month, Day) May 1988
15. PAGE COUNT 53				
16. SUPPLEMENTARY NOTATION				
17. COSATI CODES			18. SUBJECT TERMS (Continue on reverse if necessary and identify by block number)	
FIELD	GROUP	SUB-GROUP		
01	01		Navier-Stokes Equations; Computational Fluid Dynamics;	
20	04		Newton's Method (jhd)	
19. ABSTRACT (Continue on reverse if necessary and identify by block number)				
<p>A numerical procedure is presented for solution of the laminar incompressible two-dimensional Navier-Stokes equations written in terms of the stream function and vorticity. The full implicit unified method is capable of treating both steady and unsteady flows. The governing equations are solved in conservation form, incorporating a general transformation of the independent variables so that arbitrary geometrical configurations may be considered. In the steady case, the algorithm corresponds identically to Newton's method as applied to the solution of nonlinear partial differential equations. For unsteady flows, the procedure is second order accurate temporally as well as spatially. An analysis of a model system of equations is provided which indicates numerical stability. Utility of the method is verified by calculation of representative examples of both steady and unsteady flow fields. These include the classic driven cavity problem and the unsteady flow about a circular cylinder. Results of these computations are compared with previous numerical solutions as well as with experimental data.</p>				
20. DISTRIBUTION / AVAILABILITY OF ABSTRACT <input checked="" type="checkbox"/> UNCLASSIFIED/UNLIMITED <input type="checkbox"/> SAME AS RPT. <input type="checkbox"/> DTIC USERS			21. ABSTRACT SECURITY CLASSIFICATION Unclassified	
22a. NAME OF RESPONSIBLE INDIVIDUAL J. S. Shang			22b. TELEPHONE (Include Area Code) (513) 255-7127	22c. OFFICE SYMBOL AFWAL/FIMM

SUMMARY

An algorithm possessing second-order spatial accuracy has been presented for solving the laminar incompressible two-dimensional Navier-Stokes equations in streamfunction-vorticity variables. The method is either second order accurate in time for unsteady flows or corresponds to Newton's method of iteration in the steady case. The formulation is capable of handling arbitrary geometric configurations and the algorithm contains no adjustable parameters or explicitly added artificial dissipation. All terms of the governing equations are treated implicitly without incurring any factorization error as is commonly generated with alternating-direction-implicit schemes. This not only allows Newton's method to be employed for steady calculations, but also permits implicit differencing of cross-derivative terms which would arise for nonorthogonal grid systems. For the unsteady equations, an analysis of a corresponding constant coefficient system is provided which indicates numerical stability. Use of a direct solution of the linearized equations makes the method noniterative at each time step and precludes the appearance of spurious time-like terms or the possibility of a nonconverging iteration as the mesh step size is reduced. In addition, machine accuracy is not only achieved in the limit of convergence, but is also maintained at every time step. Because of the large linear system involved, extensive computing capacity is required. Example applications of the method to the driven cavity problem and to the flow about a circular cylinder have indicated the utility of the method, and results of these calculations have compared well with previous numerical solutions and with experiment.

Accession For	
NTIS GRA&I	<input checked="" type="checkbox"/>
DTIC TAB	<input type="checkbox"/>
Unannounced	<input type="checkbox"/>
Justification	
By _____	
Distribution/	
Availability Codes	
Dist	Avail and/or Special
A-1	



FOREWORD

This report is the result of research performed in the Computational Aerodynamics Group, Aerodynamic and Airframe Branch, Aeromechanics Division, Flight Dynamics Laboratory, Air Force Wright Aeronautical Laboratories, Wright-Patterson Air Force Base, Ohio 45433-6553 by Dr Donald P. Rizzetta from November 1985 to May 1987.

The author is grateful to Dr M. R. Visbal for several helpful conversations.

TABLE OF CONTENTS

<u>SECTION</u>		<u>PAGE</u>
I	INTRODUCTION	1
II	GOVERNING EQUATIONS	2
III	NUMERICAL METHOD	5
IV	STABILITY ANALYSIS	10
V	NUMERICAL EXAMPLES	14
VI	DISCUSSION	44
	REFERENCES	46

LIST OF FIGURES

<u>FIGURE</u>		<u>PAGE</u>
1	Driven Cavity Geometry and Boundary Conditions	15
2	Driven Cavity Convergence History for $R = 100$	17
3	Driven Cavity Streamfunction Contours for $R = 100$	18
4	Driven Cavity Vorticity Contours for $R = 100$	19
5	Driven Cavity Convergence History for $R = 1,000$	21
6	Driven Cavity Streamfunction Contours for $R = 1,000$	22
7	Driven Cavity Vorticity Contours for $R = 1,000$	23
8	Driven Cavity Convergence History for $R = 10,000$	24
9	Driven Cavity Streamfunction Contours for $R = 10,000$	25
10	Driven Cavity Vorticity Contours for $R = 10,000$	26
11	Comparison of Driven Cavity Velocity Profiles with Solution of Ghia, Ghia, and Shin	28
12	Circular Cylinder Computation Grid	30
13	Circular Cylinder Grid Structure at Leading Edge of Computational Domain	31
14	Circular Cylinder Boundary Conditions	33
15	Time History of Lift Coefficient for Circular Cylinder	36
16	Time History of Drag Coefficient for Circular Cylinder	37
17	Instantaneous Streamfunction Contours for Circular Cylinder	40
18	Instantaneous Vorticity Contours for Circular Cylinder	41
19	Comparison of Drag Coefficient for Circular Cylinder with Experiment	42
20	Comparison of Strouhal Number for Circular Cylinder with Experiment	43

SECTION I

INTRODUCTION

The two-dimensional laminar incompressible Navier-Stokes equations provide the proper mathematical description for a wide class of complex and practical fluid flow problems. Thus, this system has been solved numerically by a variety of techniques to obtain solutions for both steady and unsteady flows [3-8, 10, 12-15, 19]. Historically, the technical sophistication associated with these techniques has evolved in correspondence with the capability of computing hardware. Decreasing computer storage limitations and increasing central processing rates have directly promoted the emergence of new algorithms. With the advent of large scale vector-processing machines, we find it is now possible to consider procedures which were precluded by previous restrictions.

The present algorithm consists of a fully implicit finite-difference approximation to the governing partial differential equations and results in a large system of linear equations representing the dependent variables at each grid point in the computational domain. This linear system is then solved directly to either advance an unsteady solution in time or to proceed to the converged state of a steady flow. Because of the large number of linear equations which must be solved repeatedly, this formulation previously was inappropriate for implementation on computing machines having a limited capacity. When employed on the current generation of large-scale computers, however, it may not be impractical. In addition, the algorithm possesses certain inherent advantages over other methods. For unsteady problems, formal second-order temporal accuracy may be maintained. The method contains no factorization error which is commonly incurred by alternating-direction-implicit methods. By employing a direct method for solution of the linear equations, the use of relaxation parameters is avoided, along with the appearance of spurious time-like terms in the finite-difference equations. For the case of steady flows the iteration procedure corresponds directly to Newton's method for solving systems of nonlinear partial differential equations, and therefore is capable of achieving rapid rates of convergence.

SECTION II

GOVERNING EQUATIONS

For an incompressible fluid of constant properties, the nondimensional continuity and momentum equations may be written in a two-dimensional Cartesian coordinate system as

$$\frac{\partial u}{\partial x} + \frac{\partial v}{\partial y} = 0 \quad (1)$$

$$\frac{\partial u}{\partial t} + \frac{\partial}{\partial x} (u^2) + \frac{\partial}{\partial y} (uv) + \frac{\partial P}{\partial x} = \frac{1}{R} \left(\frac{\partial^2 u}{\partial x^2} + \frac{\partial^2 u}{\partial y^2} \right) \quad (2)$$

$$\frac{\partial v}{\partial t} + \frac{\partial}{\partial x} (uv) + \frac{\partial}{\partial y} (v^2) + \frac{\partial P}{\partial y} = \frac{1}{R} \left(\frac{\partial^2 v}{\partial x^2} + \frac{\partial^2 v}{\partial y^2} \right) \quad (3)$$

Here, x and y are the independent Cartesian coordinates nondimensionalized by the reference length L , and u and v are the corresponding velocity components nondimensionalized by the reference speed u_∞ . L/u_∞ has nondimensionalized the time, t , P is one-half the local pressure coefficient, and $R = u_\infty L/\mu$ is the Reynolds number. As is customary, defining a streamfunction, ψ , can satisfy the continuity equation whereby

$$u = \frac{\partial \psi}{\partial y} \quad (4)$$

$$v = -\frac{\partial \psi}{\partial x} \quad (5)$$

The pressure is eliminated by cross-differentiation of Eqs (2) and (3), and the momentum equations may be expressed in terms of the vorticity, ω , defined as

$$\omega = \frac{\partial v}{\partial x} - \frac{\partial u}{\partial y} \quad (6)$$

Thus Eqs (1)-(3) are replaced by

$$\frac{\partial \omega}{\partial t} + \frac{\partial}{\partial x} \left(\omega \frac{\partial \psi}{\partial y} \right) - \frac{\partial}{\partial y} \left(\omega \frac{\partial \psi}{\partial x} \right) = \frac{1}{R} \left(\frac{\partial^2 \omega}{\partial x^2} + \frac{\partial^2 \omega}{\partial y^2} \right) \quad (7)$$

$$\frac{\partial^2 \psi}{\partial x^2} + \frac{\partial^2 \psi}{\partial y^2} = -\omega \quad (8)$$

which are commonly referred to as the streamfunction-vorticity formulation of the Navier-Stokes equations. Equations (7) and (8) provide a concise representation of the governing equations so that any fluid flow field may be defined by the functions ψ and ω . Elimination of the pressure has reduced the number of dependent variables from three to two, thus making the equation set attractive for many numerical computations.

Since the early pioneering effort of Thom [19], relaxation procedures were employed to obtain steady flow solutions for many problems [3,4,15]. Such techniques were often slow to converge and typically reached a limit beyond which residual errors could no longer be reduced. These problems were magnified as the Reynolds number increased. An effective means of obtaining iterated solutions to the steady streamfunction-vorticity equations has more recently been achieved via Newton's method [5, 6, 13]. By solving the unsteady equations of motion it was possible to attain steady-state results in the long-time limit. Current schemes of this type can employ the alternating-direction-implicit approach [14] and multigrid algorithms [8]. In the case of nonsteady flows, early methods utilized explicit procedures for time integration [7, 10] which were subject to stability limitations. The use of upwind-differencing techniques aided in overcoming such restrictions at the expense of degraded spatial accuracy. Contemporary efficient algorithms employ an alternating-direction-implicit treatment of the vorticity transport equation coupled with a direct solution of the streamfunction equation. This approach, however, is only first order accurate in time. One obstacle associated with obtaining solutions to the unsteady equations of motion is the lack of a time derivative appearing in the streamfunction equation, thus precluding a concise representation which provides second-order temporal accuracy. Mehta and Lavan [12] resolved this difficulty by solving Eqs (7) and (8) simultaneously; however, the

method required iteration at every time step. Various other procedures exist for both the steady and unsteady equations of motion, but these are too numerous to mention here.

SECTION III

NUMERICAL METHOD

To implement the present numerical method, the Cartesian coordinates x and y are transformed to the computational system $\xi(x, y)$, $\eta(x, y)$ in the domain $0 \leq \xi \leq 1$, $0 \leq \eta \leq 1$. Here, ξ and η are boundary conforming to the particular geometry involved to consider arbitrary configurations. In addition, the computational grid is uniform in ξ and η (i.e., $\Delta\xi = \text{constant}$, $\Delta\eta = \text{constant}$) so that all spatial derivatives may be approximated by simple second-order accurate finite-difference expressions, as is customary. Under this transformation, the governing equations are written in conservative form as

$$\frac{\partial}{\partial t} \left(\frac{\omega}{J} \right) + \frac{\partial}{\partial \xi} \left(\omega \frac{\partial \psi}{\partial \eta} \right) - \frac{\partial}{\partial \eta} \left(\omega \frac{\partial \psi}{\partial \xi} \right) - \frac{1}{R} \left\{ \frac{\partial}{\partial \xi} \left[\left(\frac{\xi_x^2 + \xi_y^2}{J} \right) \frac{\partial \omega}{\partial \xi} \right] + \frac{\partial}{\partial \eta} \left[\left(\frac{\eta_x^2 + \eta_y^2}{J} \right) \frac{\partial \omega}{\partial \eta} \right] \right\} = 0 \quad (9)$$

$$\frac{\partial}{\partial \xi} \left[\left(\frac{\xi_x^2 + \xi_y^2}{J} \right) \frac{\partial \psi}{\partial \xi} \right] + \frac{\partial}{\partial \eta} \left[\left(\frac{\eta_x^2 + \eta_y^2}{J} \right) \frac{\partial \psi}{\partial \eta} \right] = - \frac{\omega}{J} \quad (10)$$

where ξ_x , ξ_y , η_x , η_y are the metric coefficients and $J = \xi_x \eta_y - \xi_y \eta_x$ is the Jacobian of the transformation. For convenience we assume that ξ and η are orthogonal, although this simplification is not fundamental to the method. We now presume that ψ and ω are known at time level t^n or at the n -th iteration and Eqs (9) and (10) are used to advance the solution to the $n+1$ level. Approximating Eq (9) accomplishes this at the $n+1/2$ time level for the unsteady equation or at the $n+1$ iteration if $\frac{\partial \omega}{\partial t} = 0$. For either situation, Eq (10) is satisfied at the $n+1$ level. Upon introducing the "delta form" of the dependent variables [2], i.e., $\Delta\psi = \psi^{n+1} - \psi^n$, $\Delta\omega = \omega^{n+1} - \omega^n$, into the governing equations and neglecting terms of order Δ^2 , Eqs (9) and (10) are expressed as

$$\begin{aligned} & \left(\frac{\epsilon}{\Delta t} \right) \frac{\Delta\omega}{J} + \left(1 - \frac{\epsilon}{2} \right) \left\{ \frac{\partial}{\partial \xi} \left(\omega^n \frac{\partial \Delta\psi}{\partial \eta} + \frac{\partial \psi^n}{\partial \eta} \Delta\omega \right) - \frac{\partial}{\partial \eta} \left(\omega^n \frac{\partial \Delta\psi}{\partial \xi} + \frac{\partial \psi^n}{\partial \xi} \Delta\omega \right) \right. \\ & \quad \left. - \frac{1}{R} \frac{\partial}{\partial \xi} \left[\left(\frac{\xi_x^2 + \xi_y^2}{J} \right) \frac{\partial \Delta\omega}{\partial \xi} \right] - \frac{1}{R} \frac{\partial}{\partial \eta} \left[\left(\frac{\eta_x^2 + \eta_y^2}{J} \right) \frac{\partial \Delta\omega}{\partial \eta} \right] \right\} \\ & = - \frac{\partial}{\partial \xi} \left(\omega^n \frac{\partial \psi^n}{\partial \eta} \right) + \frac{\partial}{\partial \eta} \left(\omega^n \frac{\partial \psi^n}{\partial \xi} \right) + \frac{1}{R} \left\{ \frac{\partial}{\partial \xi} \left[\left(\frac{\xi_x^2 + \xi_y^2}{J} \right) \frac{\partial \omega^n}{\partial \xi} \right] \right. \\ & \quad \left. + \frac{\partial}{\partial \eta} \left[\left(\frac{\eta_x^2 + \eta_y^2}{J} \right) \frac{\partial \omega^n}{\partial \eta} \right] \right\} \end{aligned} \quad (11)$$

$$\begin{aligned}
& \frac{\partial}{\partial \xi} \left[\left(\frac{\xi_x^2 + \xi_y^2}{J} \right) \frac{\partial \Delta \psi}{\partial \xi} \right] + \frac{\partial}{\partial \eta} \left[\left(\frac{\eta_x^2 + \eta_y^2}{J} \right) \frac{\partial \Delta \psi}{\partial \eta} \right] + \frac{\Delta \omega}{J} \\
& = - \frac{\partial}{\partial \xi} \left[\left(\frac{\xi_x^2 + \xi_y^2}{J} \right) \frac{\partial \psi^n}{\partial \xi} \right] - \frac{\partial}{\partial \eta} \left[\left(\frac{\eta_x^2 + \eta_y^2}{J} \right) \frac{\partial \psi^n}{\partial \eta} \right] - \frac{\omega^n}{J}
\end{aligned} \tag{12}$$

where $\epsilon = 1$ for unsteady flow and $\epsilon = 0$ for steady flow. Equations (11) and (12) are solved repeatedly at each time step or iteration to obtain $\Delta \psi$ and $\Delta \omega$, the values of ψ and ω are updated, and the procedure is repeated to advance the solution. The unified formulation expressed by Eqs (11) and (12) is either second order accurate in time for nonsteady flows or corresponds to Newton's method of iteration for solving nonlinear partial differential equations [11] in the stationary case.

All spatial derivatives appearing in Eqs (11) and (12) are approximated by their common centered second-order accurate finite-difference representations in terms of the dependent variables at each grid point (i, j) of the computational mesh, where for example $\psi_{i,j} = \psi(\xi_i, \eta_j)$. By defining

$$X = \left(\frac{1}{\Delta \xi} \right)^2 \left(\frac{\xi_x^2 + \xi_y^2}{J} \right) \tag{13}$$

$$Y = \left(\frac{1}{\Delta \eta} \right)^2 \left(\frac{\eta_x^2 + \eta_y^2}{J} \right) \tag{14}$$

$$\alpha = \frac{(2 - \epsilon) R}{4 \Delta \xi \Delta \eta} \tag{15}$$

$$\beta = 1 - \frac{\epsilon}{2} \tag{16}$$

$$\gamma = \frac{R}{2 \Delta \xi \Delta \eta} \tag{17}$$

the vorticity transport equation becomes

$$\begin{aligned}
 & \alpha \left[(\omega_{i-1, j}^n - \omega_{i, j-1}^n) \Delta \psi_{i-1, j-1} + (\omega_{i, j+1}^n - \omega_{i-1, j}^n) \Delta \psi_{i-1, j+1} \right. \\
 & \quad \left. + (\omega_{i, j-1}^n - \omega_{i+1, j}^n) \Delta \psi_{i+1, j-1} + (\omega_{i+1, j}^n - \omega_{i, j+1}^n) \Delta \psi_{i+1, j+1} \right] \\
 & + \left[\alpha (\psi_{i-1, j-1}^n - \psi_{i-1, j+1}^n) - \beta (X_{i, j} + X_{i-1, j}) \right] \Delta \omega_{i-1, j} \\
 & + \left[\alpha (\psi_{i+1, j-1}^n - \psi_{i-1, j-1}^n) - \beta (Y_{i, j} + Y_{i, j-1}) \right] \Delta \omega_{i, j-1} \\
 & + \left[\frac{2\epsilon R}{\Delta t J_{i, j}} + \beta (X_{i+1, j} + 2X_{i, j} + X_{i-1, j} + Y_{i, j+1} + 2Y_{i, j} + Y_{i, j-1}) \right] \Delta \omega_{i, j} \\
 & + \left[\alpha (\psi_{i-1, j+1}^n - \psi_{i+1, j+1}^n) - \beta (Y_{i, j+1} + Y_{i, j}) \right] \Delta \omega_{i, j+1} \\
 & + \left[\alpha (\psi_{i+1, j+1}^n - \psi_{i+1, j-1}^n) - \beta (X_{i+1, j} + X_{i, j}) \right] \Delta \omega_{i+1, j} \\
 & = \gamma \left[(\psi_{i-1, j+1}^n - \psi_{i-1, j-1}^n) \omega_{i-1, j}^n - (\psi_{i+1, j-1}^n - \psi_{i-1, j-1}^n) \omega_{i, j-1}^n \right. \\
 & \quad + (\psi_{i+1, j+1}^n - \psi_{i-1, j+1}^n) \omega_{i, j+1}^n - (\psi_{i+1, j+1}^n - \psi_{i+1, j-1}^n) \omega_{i+1, j}^n \\
 & \quad + (X_{i, j} + X_{i-1, j}) \omega_{i-1, j}^n + (Y_{i, j} + Y_{i, j-1}) \omega_{i, j-1}^n \\
 & \quad - (X_{i+1, j} + 2X_{i, j} + X_{i-1, j} + Y_{i, j+1} + 2Y_{i, j} + Y_{i, j-1}) \omega_{i, j}^n \\
 & \quad \left. + (Y_{i, j+1} + Y_{i, j}) \omega_{i, j+1}^n + (X_{i+1, j} + X_{i, j}) \omega_{i+1, j}^n \right]
 \end{aligned}
 \tag{18}$$

Similarly, the streamfunction equation is

$$\begin{aligned}
 & (X_{i,j} + X_{i-1,j}) \Delta\psi_{i-1,j} + (Y_{i,j} + Y_{i,j-1}) \Delta\psi_{i,j-1} \\
 & - (X_{i+1,j} + 2X_{i,j} + X_{i-1,j} + Y_{i,j+1} + 2Y_{i,j} + Y_{i,j-1}) \Delta\psi_{i,j} \\
 & + (Y_{i,j+1} + Y_{i,j}) \Delta\psi_{i,j+1} + (X_{i+1,j} + X_{i,j}) \Delta\psi_{i+1,j} + \left(\frac{2}{J_{i,j}}\right) \Delta\omega_{i,j} \\
 & = (X_{i,j} + X_{i-1,j}) (\psi_{i,j}^n - \psi_{i-1,j}^n) - (X_{i+1,j} + X_{i,j}) (\psi_{i+1,j}^n - \psi_{i,j}^n) \\
 & + (Y_{i,j} + Y_{i,j-1}) (\psi_{i,j}^n - \psi_{i,j-1}^n) - (Y_{i,j+1} + Y_{i,j}) (\psi_{i,j+1}^n - \psi_{i,j}^n) - \left(\frac{2}{J_{i,j}}\right) \omega_{i,j}^n
 \end{aligned} \tag{19}$$

Equations (18) and (19) represent the linear system which must be solved for all $\Delta\psi_{i,j}$, $\Delta\omega_{i,j}$ at each time step. If the computational domain consists of (I, J) grid points in (ξ, η) respectively, then the system, including boundary conditions, is comprised of $2IJ$ equations for the variables $\Delta\psi_{i,j}$, $\Delta\omega_{i,j}$ where $1 \leq i \leq I$ and $1 \leq j \leq J$. This system may be expressed notationally by the matrix equation

$$M \vec{Z} = \vec{r} \tag{20}$$

where M is a square matrix of dimension $(2IJ \times 2IJ)$, and the solution \vec{Z} and right-hand-side \vec{r} are vectors of length $(2IJ)$. Although the matrix M is large, it is quite sparse. Thus, we do not find it necessary to store a vast number of coefficients to solve the linear system. In addition, M is rich in structure so that a direct solution to Eq (20) may be obtained by efficient means. Various forms for the matrix M are possible depending upon how the equations are ordered. For the moment, if we consider Dirichlet conditions at all computational boundaries and let

$$\begin{aligned}
 \vec{Z} = \{ & [(\Delta\psi_{1,1} \Delta\omega_{1,1}) \dots (\Delta\psi_{1,j} \Delta\omega_{1,j}) \dots (\Delta\psi_{1,J} \Delta\omega_{1,J})] [(\Delta\psi_{2,1} \Delta\omega_{2,1}) \dots \\
 & \dots (\Delta\psi_{I-1,J} \Delta\omega_{I-1,J})] [(\Delta\psi_{I,1} \Delta\omega_{I,1}) \dots (\Delta\psi_{I,j} \Delta\omega_{I,j}) \dots (\Delta\psi_{I,J} \Delta\omega_{I,J})] \}^T \tag{21}
 \end{aligned}$$

then M has the block-tridiagonal form

$$M = \begin{bmatrix} D_1 & E_1 & & & \\ C_2 & D_2 & E_2 & & \\ & \ddots & \ddots & \ddots & \\ & & C_{I-1} & D_{I-1} & E_{I-1} \\ & & & C_I & D_I \end{bmatrix} \quad (22)$$

Here the blocks C_i , D_i , and E_i are $(2J \times 2J)$ square matrices which are also sparse. Each block itself has a block-tridiagonal substructure comprised of (2×2) square blocks. Equivalently, the C_i , D_i , and E_i matrices may be considered heptadiagonal. Fornberg [5, 6] presents an alternative structure for the matrix M by considering a different ordering of the solution vector \vec{z} .

The linear system represented by Eq (20) is solved by a direct method. A noniterative technique is essential and should be free from limitations of convergence as the mesh size is refined. In addition, a high order of accuracy can be obtained in the solution at each time step, and spurious time-like relaxation errors will be precluded. We emphasize that the specific technique employed to solve the linear system is not basic to the numerical method. Many efficient solution procedures are available for this purpose. For the present results, which serve only as illustrative examples, a block-Gaussian elimination [9] was implemented where C_i , D_i , and E_i were considered as full matrices without further simplification.

SECTION IV

STABILITY ANALYSIS

For the steady case ($\epsilon = 0$), because the algorithm corresponds to Newton's method, convergence of the solution is guaranteed provided the initial iterate is sufficiently close to the desired root. Mathematical proof of this property exists [9] so that no further analysis of convergence is required. In addition, since Newton iteration is a second-order method, the approach to the steady state is quadratic, i.e., $\Delta\psi^{n+1} = O(\Delta\psi^n)^2$. For the unsteady case ($\epsilon = 1$), stability of the procedure may be investigated by considering a linear model system of equations with constant coefficients. While the stability of linear constant coefficient systems is neither a necessary nor sufficient condition for the stability of corresponding nonlinear systems, it can serve as a guide for stability in the nonlinear situation.

Equations (7) and (8) are modeled by the linear system

$$\frac{\partial\omega}{\partial t} + a_1 \frac{\partial\psi}{\partial x} + a_2 \frac{\partial\psi}{\partial y} + b_1 \frac{\partial\omega}{\partial x} + b_2 \frac{\partial\omega}{\partial y} = \frac{1}{R} \left(\frac{\partial^2\omega}{\partial x^2} + \frac{\partial^2\omega}{\partial y^2} \right) \quad (23)$$

$$\frac{\partial^2\psi}{\partial x^2} + \frac{\partial^2\psi}{\partial y^2} + \omega = 0 \quad (24)$$

where a_1, a_2, b_1, b_2 , are real constant coefficients. The finite-difference representations of these equations, which corresponds to the method described in the previous section, are expressed notationally as

$$\begin{aligned} \frac{\omega^{n+1} - \omega^n}{\Delta t} + (a_1 \delta_x + a_2 \delta_y) \left(\frac{\psi^{n+1} + \psi^n}{2} \right) + (b_1 \delta_x + b_2 \delta_y) \left(\frac{\omega^{n+1} + \omega^n}{2} \right) \\ = \frac{1}{R} (\delta_{xx} + \delta_{yy}) \left(\frac{\omega^{n+1} + \omega^n}{2} \right) \end{aligned} \quad (25)$$

$$(\delta_{xx} + \delta_{yy}) \psi^{n+1} + \omega^{n+1} = 0 \quad (26)$$

Here δ_x , δ_y , δ_{xx} , δ_{yy} , are the common centered second-order accurate finite-difference operators. Because the system is linear, the "delta" form of the equations will be identical to Eqs (25) and (26) but has been omitted for convenience. Upon defining

$$\alpha_1 = \frac{a_1 \Delta t}{2}, \alpha_2 = \frac{a_2 \Delta t}{2}, \beta_1 = \frac{b_1 \Delta t}{2}, \beta_2 = \frac{b_2 \Delta t}{2}, \gamma = \frac{\Delta t}{2R} \quad (27)$$

the system may be written as

$$\begin{aligned} & (\alpha_1 \delta_x + \alpha_2 \delta_y) \psi^{n+1} + [1 + (\beta_1 \delta_x + \beta_2 \delta_y) - \gamma (\delta_{xx} + \delta_{yy})] \omega^{n+1} \\ & = - (\alpha_1 \delta_x + \alpha_2 \delta_y) \psi^n + [1 - (\beta_1 \delta_x + \beta_2 \delta_y) + \gamma (\delta_{xx} + \delta_{yy})] \omega^n \end{aligned} \quad (28)$$

$$(\delta_{xx} + \delta_{yy}) \psi^{n+1} + \omega^{n+1} = 0 \quad (29)$$

where we note that $\gamma \geq 0$.

The algorithm represented by Eqs (28) and (29) is now analyzed for stability by the standard von Neuman technique. We assume that the difference equations are to be solved on a finite computational domain with the uniform grid spacings Δx , Δy . Owing to the fact that the system is linear, ψ and ω may be expressed as complex Fourier series of the form

$$\psi(x, y, t) = \sum_{k=0}^{\infty} \sum_{l=0}^{\infty} A_{kl}(t) e^{i(\theta_k x + \phi_l y)} \quad (30)$$

$$\omega(x, y, t) = \sum_{k=0}^{\infty} \sum_{l=0}^{\infty} B_{kl}(t) e^{i(\theta_k x + \phi_l y)} \quad (31)$$

where $i = \sqrt{-1}$, A_{k1} and B_{k1} are the Fourier coefficients, and $\theta_k = \frac{2\pi k}{L_1}$, $\phi_1 = \frac{2\pi l}{L_2}$, for the region $0 \leq x \leq L_1$, $0 \leq y \leq L_2$. Substitution of (30) and (31) into (28) leads to the following result:

$$\begin{aligned}
 & \sum_{k=0}^{\infty} \sum_{l=0}^{\infty} \left[\left(\frac{\alpha_1}{\Delta x} \right) \sin(\theta_k \Delta x) + \left(\frac{\alpha_2}{\Delta y} \right) \sin(\phi_1 \Delta y) \right] i A_{k1}^{n+1} e^{i(\theta_k x + \phi_1 y)} \\
 & + \sum_{k=0}^{\infty} \sum_{l=0}^{\infty} \left\{ 1 + \gamma \left[\left(\frac{2}{\Delta x} \right)^2 \sin^2 \left(\frac{\theta_k \Delta x}{2} \right) + \left(\frac{2}{\Delta y} \right)^2 \sin^2 \left(\frac{\phi_1 \Delta y}{2} \right) \right] \right. \\
 & \left. + \left[\left(\frac{\beta_1}{\Delta x} \right) \sin(\theta_k \Delta x) + \left(\frac{\beta_2}{\Delta y} \right) \sin(\phi_1 \Delta y) \right] i \right\} B_{k1}^{n+1} e^{i(\theta_k x + \phi_1 y)} \\
 & = \sum_{k=0}^{\infty} \sum_{l=0}^{\infty} - \left[\left(\frac{\alpha_1}{\Delta x} \right) \sin(\theta_k \Delta x) + \left(\frac{\alpha_2}{\Delta y} \right) \sin(\phi_1 \Delta y) \right] i A_{k1}^n e^{i(\theta_k x + \phi_1 y)} \\
 & + \sum_{k=0}^{\infty} \sum_{l=0}^{\infty} \left\{ 1 - \gamma \left[\left(\frac{2}{\Delta x} \right)^2 \sin^2 \left(\frac{\theta_k \Delta x}{2} \right) + \left(\frac{2}{\Delta y} \right)^2 \sin^2 \left(\frac{\phi_1 \Delta y}{2} \right) \right] \right. \\
 & \left. - \left[\left(\frac{\beta_1}{\Delta x} \right) \sin(\theta_k \Delta x) + \left(\frac{\beta_2}{\Delta y} \right) \sin(\phi_1 \Delta y) \right] i \right\} B_{k1}^n e^{i(\theta_k x + \phi_1 y)} \quad (32)
 \end{aligned}$$

Due to the orthogonality of the eigenfunctions in the series, Eq (32) can be satisfied only if the coefficient of each eigenfunction vanishes identically, so that the coefficients are related according to the expression

$$\mu_1 i A_{k1}^{n+1} + (1 + \gamma\sigma + \mu_2 i) B_{k1}^{n+1} = -\mu_1 i A_{k1}^n + (1 - \gamma\sigma - \mu_2 i) B_{k1}^n \quad (33)$$

where μ_1 , μ_2 , and σ are real and $\sigma \geq 0$. Similarly, if Eqs (30) and (31) are substituted into Eq (29), and orthogonality is invoked, there results

$$-\left[\left(\frac{2}{\Delta x} \right)^2 \sin^2 \left(\frac{\theta_k \Delta x}{2} \right) + \left(\frac{2}{\Delta y} \right)^2 \sin^2 \left(\frac{\phi_1 \Delta y}{2} \right) \right] A_{k1}^{n+1} + B_{k1}^{n+1} = 0 \quad (34)$$

or

$$\sigma A_{k1}^{n+1} = B_{k1}^{n+1} \quad (35)$$

which also implies

$$\sigma A_{k1}^n = B_{k1}^n \quad (36)$$

Substitution of Eqs (35) and (36) into Eq (33) leads to

$$\mu_1 i A_{k1}^{n+1} + (1 + \gamma\sigma + \mu_2 i)\sigma A_{k1}^{n+1} = -\mu_1 i A_{k1}^n + (1 - \gamma\sigma - \mu_2 i)\sigma A_{k1}^n \quad (37)$$

Equation (37) is of the form

$$[\sigma(1 + \gamma\sigma) + \lambda i] A_{k1}^{n+1} = [\sigma(1 - \gamma\sigma) - \lambda i] A_{k1}^n \quad (38)$$

where λ is real. The amplification factor, g , is then given by

$$g = \left| \frac{A_{k1}^{n+1}}{A_{k1}^n} \right| = \left[\frac{\sigma^2 (1 - \gamma\sigma)^2 + \lambda^2}{\sigma^2 (1 + \gamma\sigma)^2 + \lambda^2} \right]^{1/2} \quad (39)$$

Recalling that $\gamma, \sigma \geq 0$, it follows that $g \leq 1$ for all $\Delta x, \Delta y, \Delta t$, and R which is the criterion for stability. Note that (35), (36), and (39) also imply

$$\left| \frac{B_{k1}^{n+1}}{B_{k1}^n} \right| \quad (40)$$

SECTION V

NUMERICAL EXAMPLES

To demonstrate the application of the present algorithm to the solution of physical problems, several numerical examples are computed. These include the classic driven cavity problem and the flow about a circular cylinder, which exhibits unsteady vortex shedding. Selection of these examples was motivated by a desire to illustrate the computation of both steady and unsteady flow fields and to provide comparison with previous calculations and with experiment. Note that for all of the results presented here the metric coefficients were evaluated numerically by second-order accurate formulae which correspond to centered differences at all interior grid nodes and three-point one-sided differences at computational boundaries. By employing the relationships

$$J = \frac{1}{x_{\xi} y_{\eta} - x_{\eta} y_{\xi}} \quad (41)$$

$$\xi_x = y_{\eta} J, \xi_y = -x_{\eta} J, \eta_x = -y_{\xi} J, \eta_y = x_{\xi} J \quad (42)$$

these differences were carried out on the computational grid (ξ, η) as is conventional.

Driven Cavity

Since the first solutions were produced by Burggraf [3], flow in a driven cavity has served as an example for the validation of many algorithms. The reasons that this problem is attractive are that the geometry is simple, a Cartesian grid system is optimal, and the resulting solutions exemplify nonlinear fluid behavior, including reversed flow regions. Figure 1 depicts a square cavity with sides of length L and with the origin located at the lower left-hand corner. The upper boundary is moving from left to right with the reference speed u_{∞} . Boundary conditions on the solid walls consist of the definition of the reference streamline and the no slip condition for the velocity components. The corresponding boundary conditions for vorticity are in fact the compatibility relations obtained by employing the limiting values of the velocity components in the vorticity definition (Eq (12)) at the walls. A second-order accurate spatial representation of these conditions results in four-point one-sided differences. While implementation of the

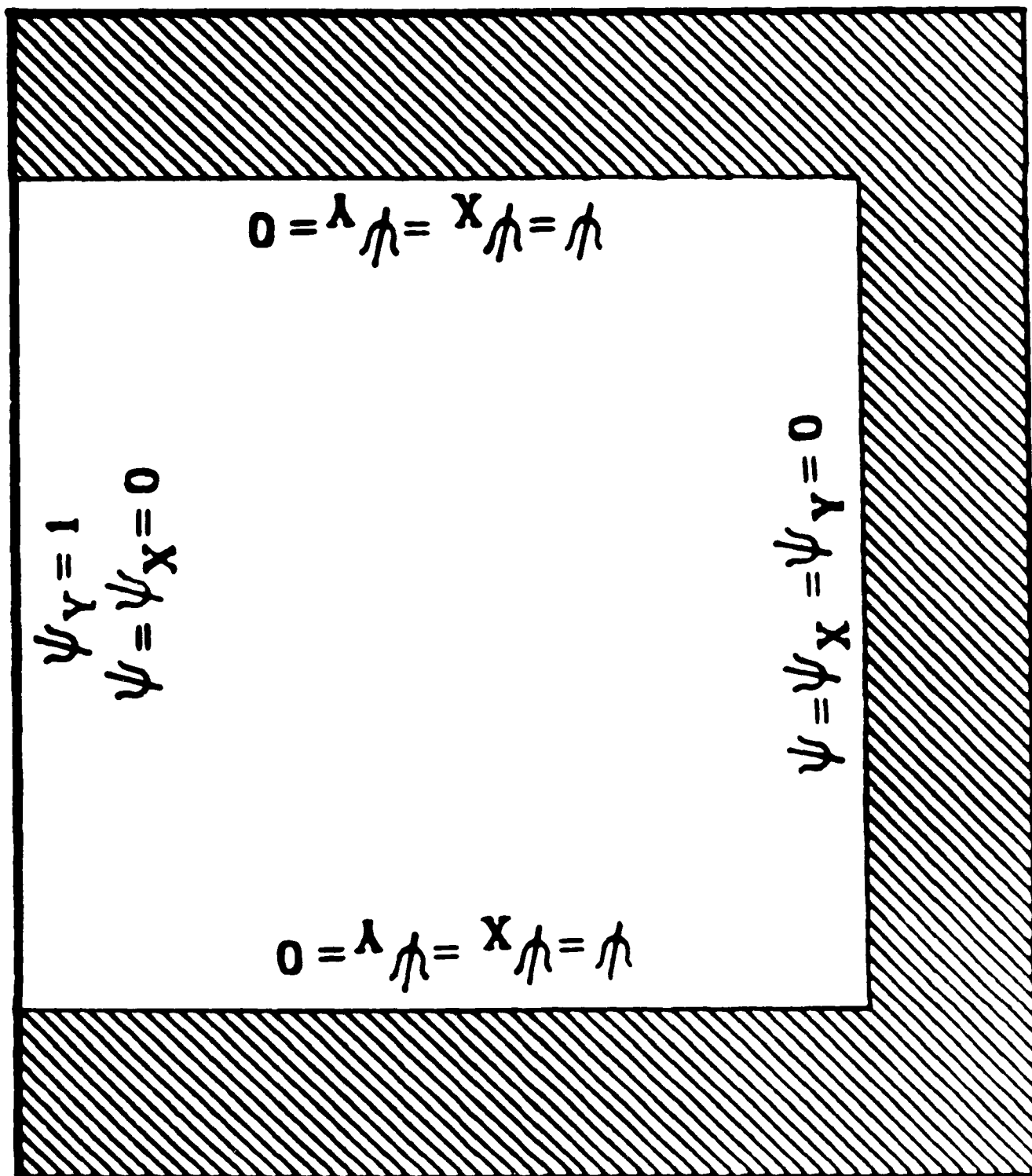


Figure 1. Driven Cavity Geometry and Boundary Conditions

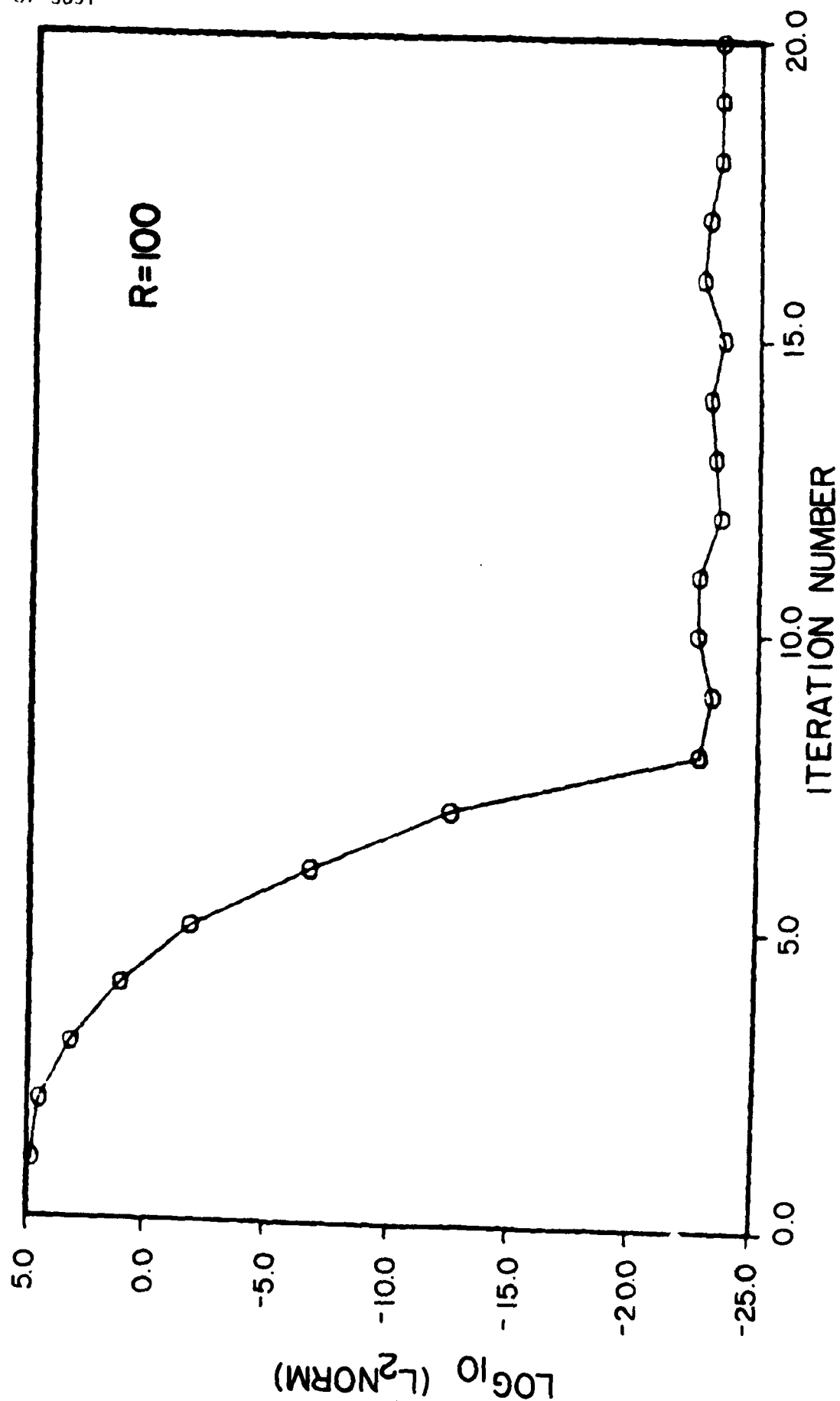


Figure 2. Driven Cavity Convergence History for R = 100

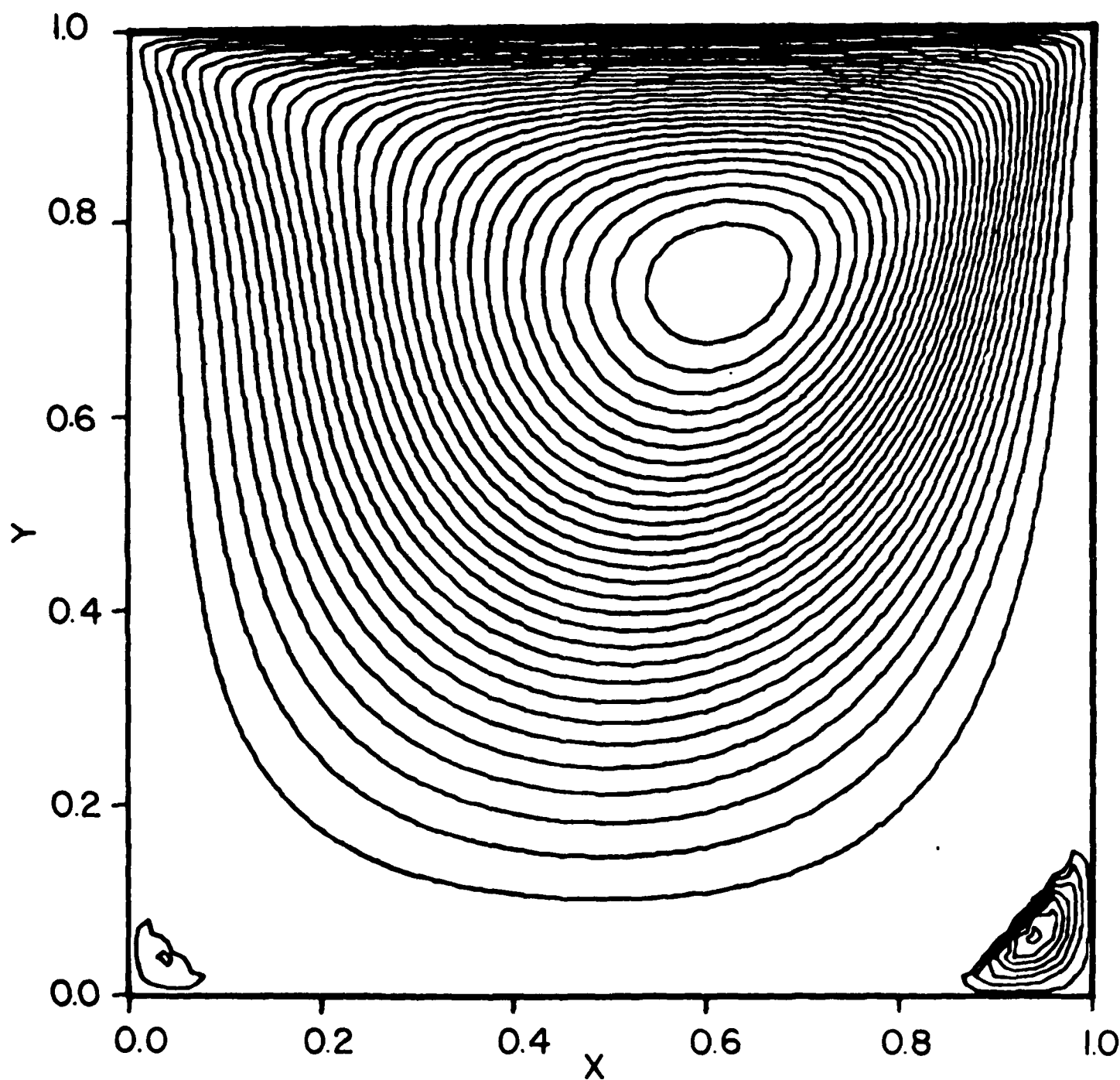


Figure 3. Driven Cavity Streamfunction Contours for $R = 100$

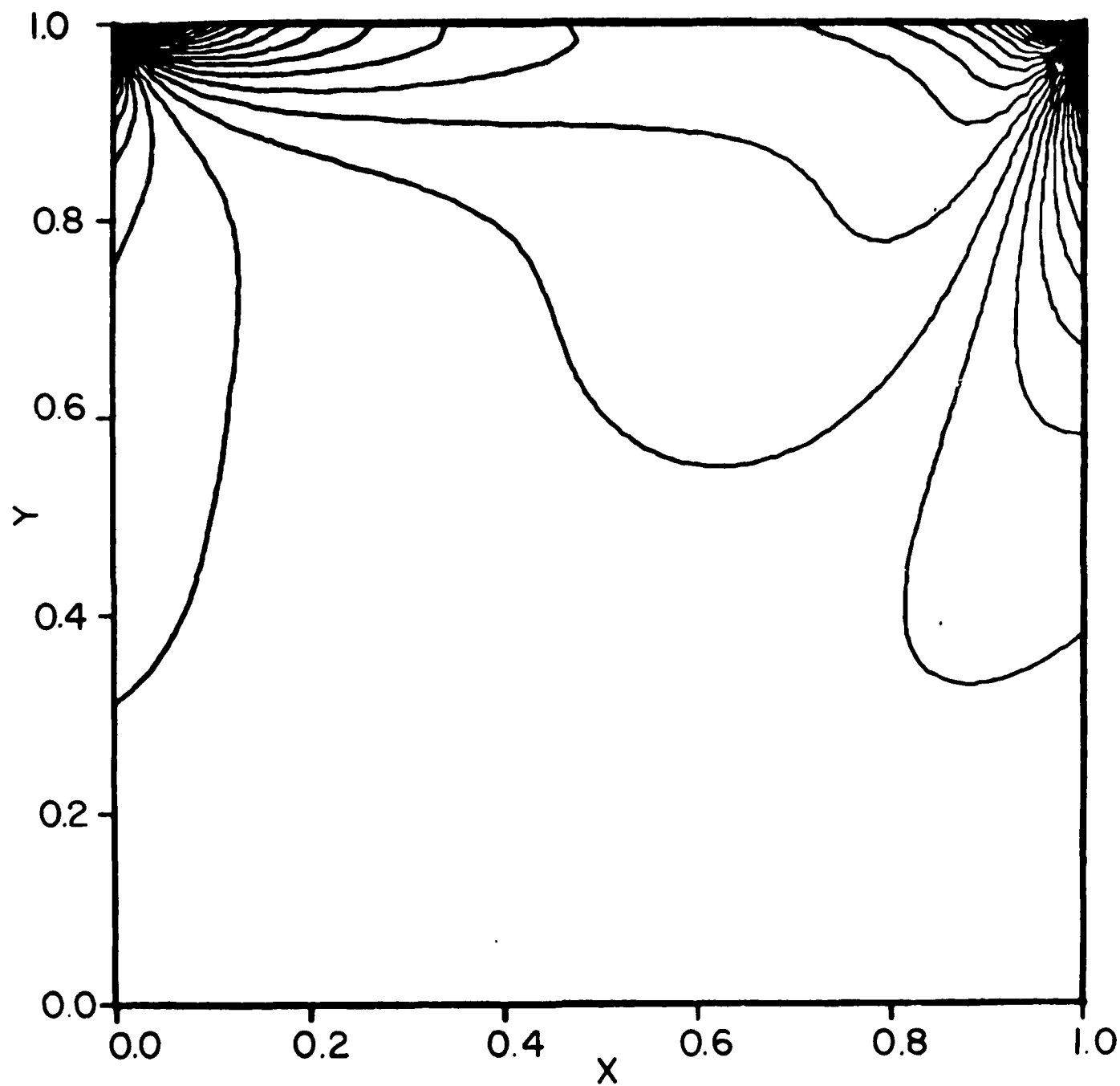
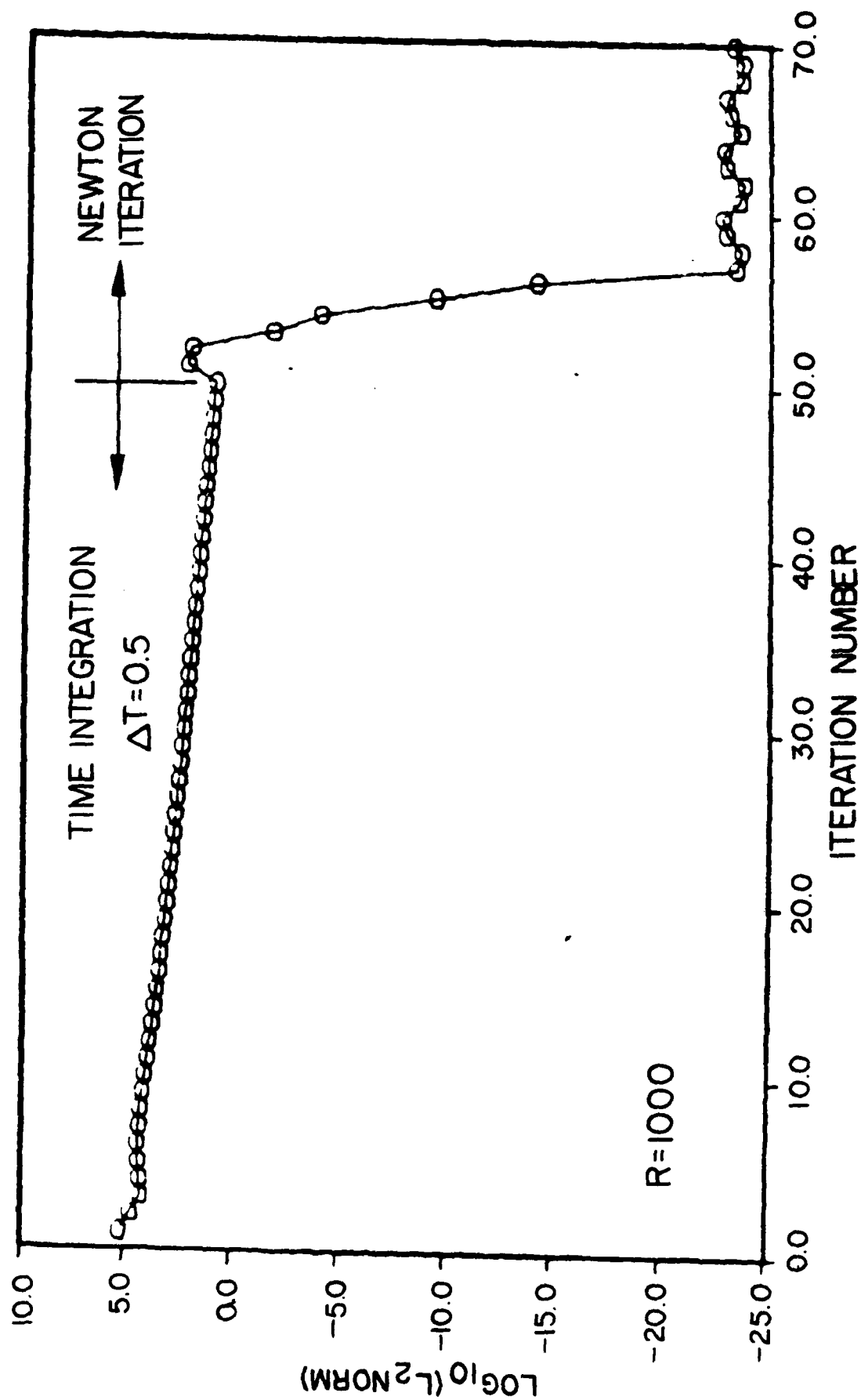


Figure 4. Driven Cavity Vorticity Contours for $R = 100$

As indicated in Fig. 2, the Newton method is always capable of attaining a quadratic rate of convergence if the initial solution is sufficiently close to the final state. For arbitrary fluid flow problems it is not usually possible to determine initial solutions which satisfy this condition a priori. In the case of the driven cavity with $R = 1,000$, the Newton method did not converge when homogeneous initial conditions were employed. If, however, the solution was allowed to evolve from the initial homogeneous state by time integration for 50 time steps with $\Delta t = 0.5$, machine accuracy could then be attained in an additional seven steps of Newton iteration. The procedure of time integration augmented by iteration illustrates the utility of the unified algorithm. As an alternative approach, Fornberg [5, 6] computed the steady symmetric flow about a circular cylinder obtained via Newton's method by generating a series of solutions with increasing Reynolds number, where each new converged result served as the initial solution for the next higher value of R .

The convergence history for $R = 1,000$ appears in Fig. 5. Streamfunction contours for this case are displayed in Fig. 6. Note that the vortex core is located more toward the center of the cavity than was the case for $R = 100$. In addition the regions of secondary flow in the lower corners are more extensive. Although not discernable in the figure, a secondary flow region is also present in the upper left-hand corner. Corresponding contours of the vorticity are shown in Fig. 7.

A more severe test of the method presented here is the driven cavity problem for a Reynolds number of 10,000. In this case, the converged result for $R = 1,000$ was employed as the initial profile and the solution was evolved in the time accurate mode for 250 steps with $\Delta t = 0.1$. At this point the solution was sufficiently close to the final state so that convergence to machine accuracy was obtained with less than an additional 15 steps of Newton iteration. The convergence history of this calculation is presented in Fig. 8. Resulting streamfunction contours are shown in Fig. 9 and indicate that the vortex core has continued to move toward the center of the cavity as the Reynolds number is increased. We also note that the lower right-hand secondary region has decreased in extent, while those in the upper and lower left-hand corners have increased. The corresponding vorticity contours shown in Fig. 10 indicate regions of extremely high-vorticity gradient

Figure 5. Driven Cavity Convergence History for $R = 1,000$

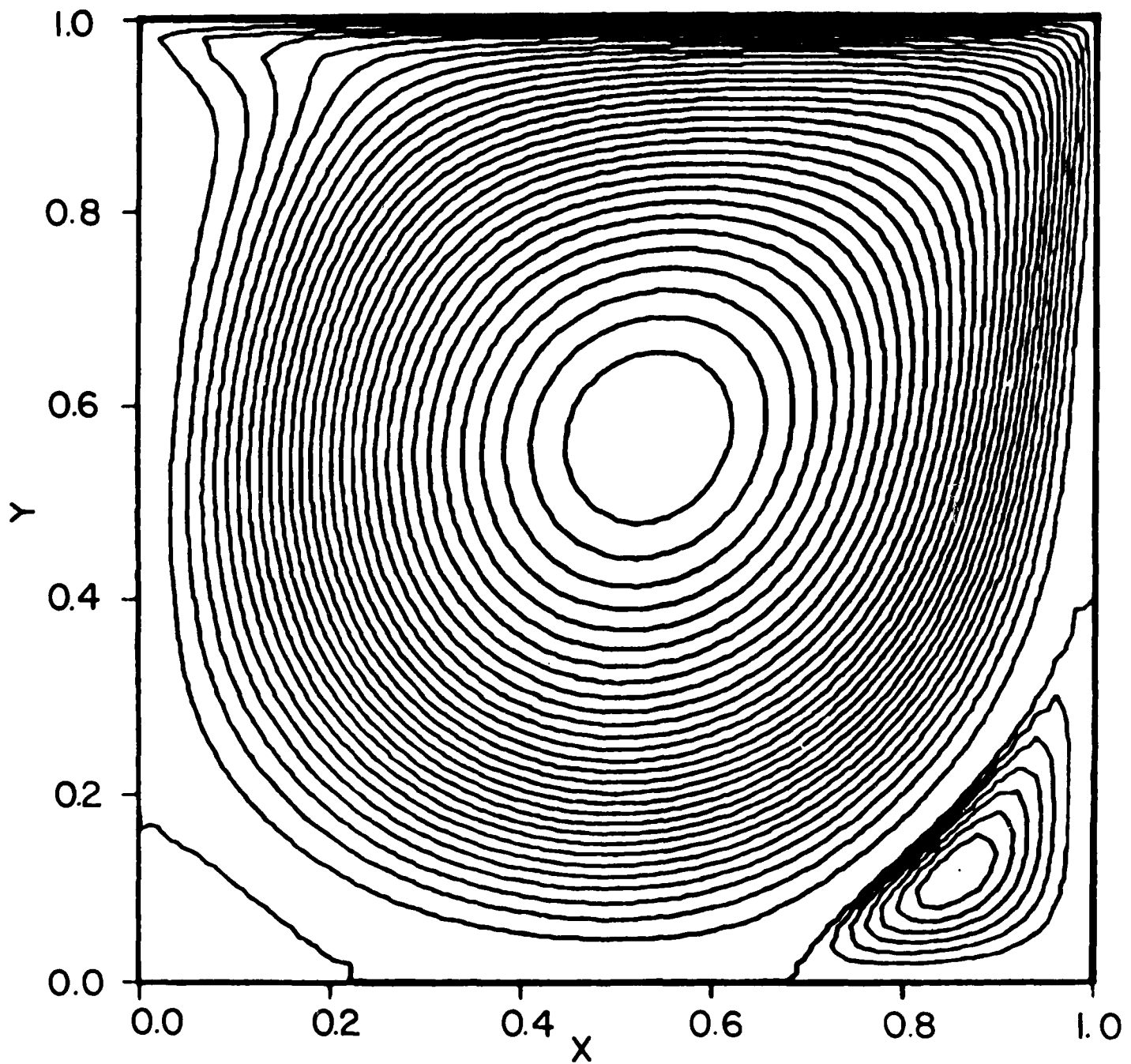


Figure 6. Driven Cavity Streamfunction Contours for $R = 1,000$

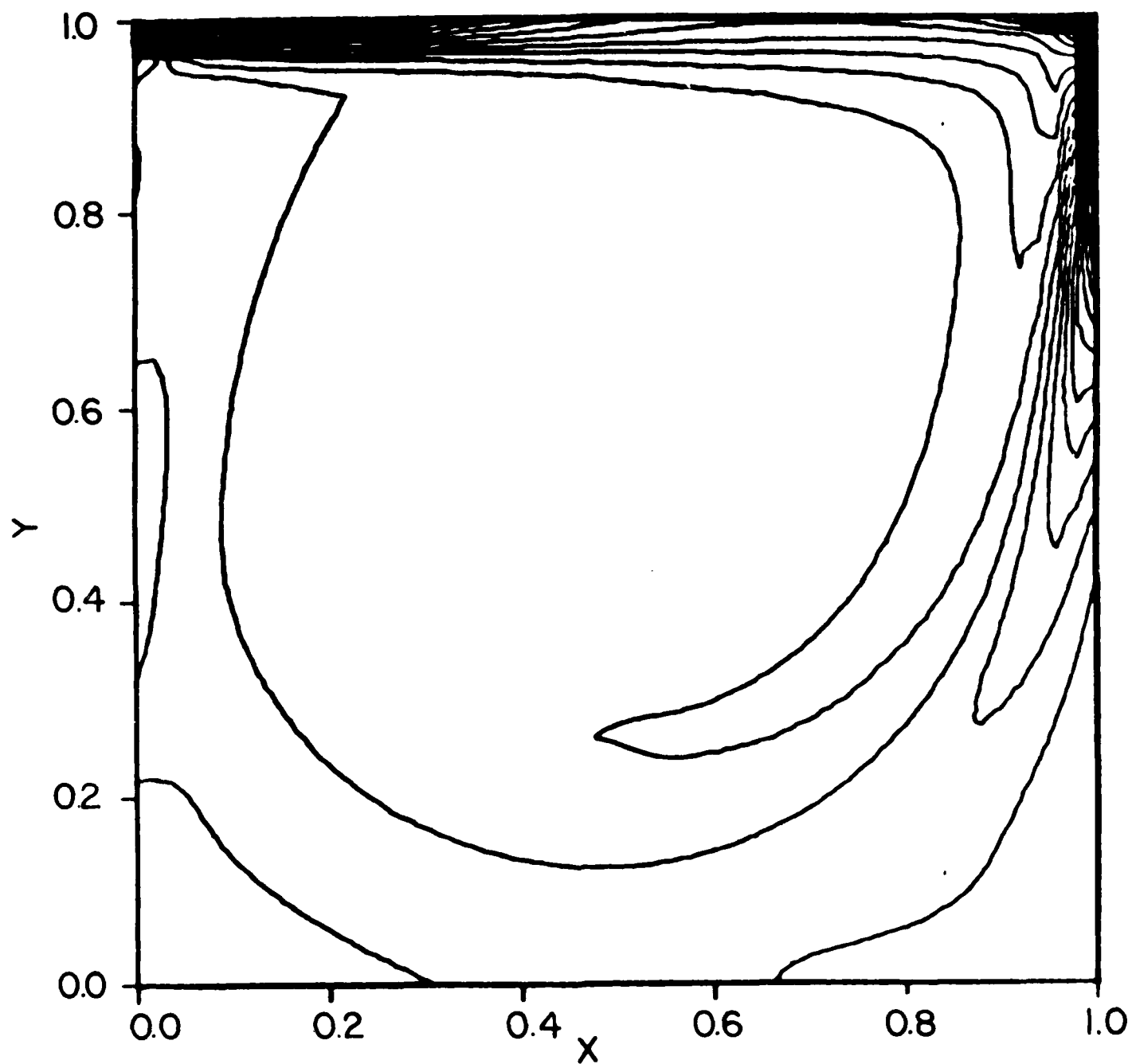


Figure 7. Driven Cavity Vorticity Contours for $R = 1,000$

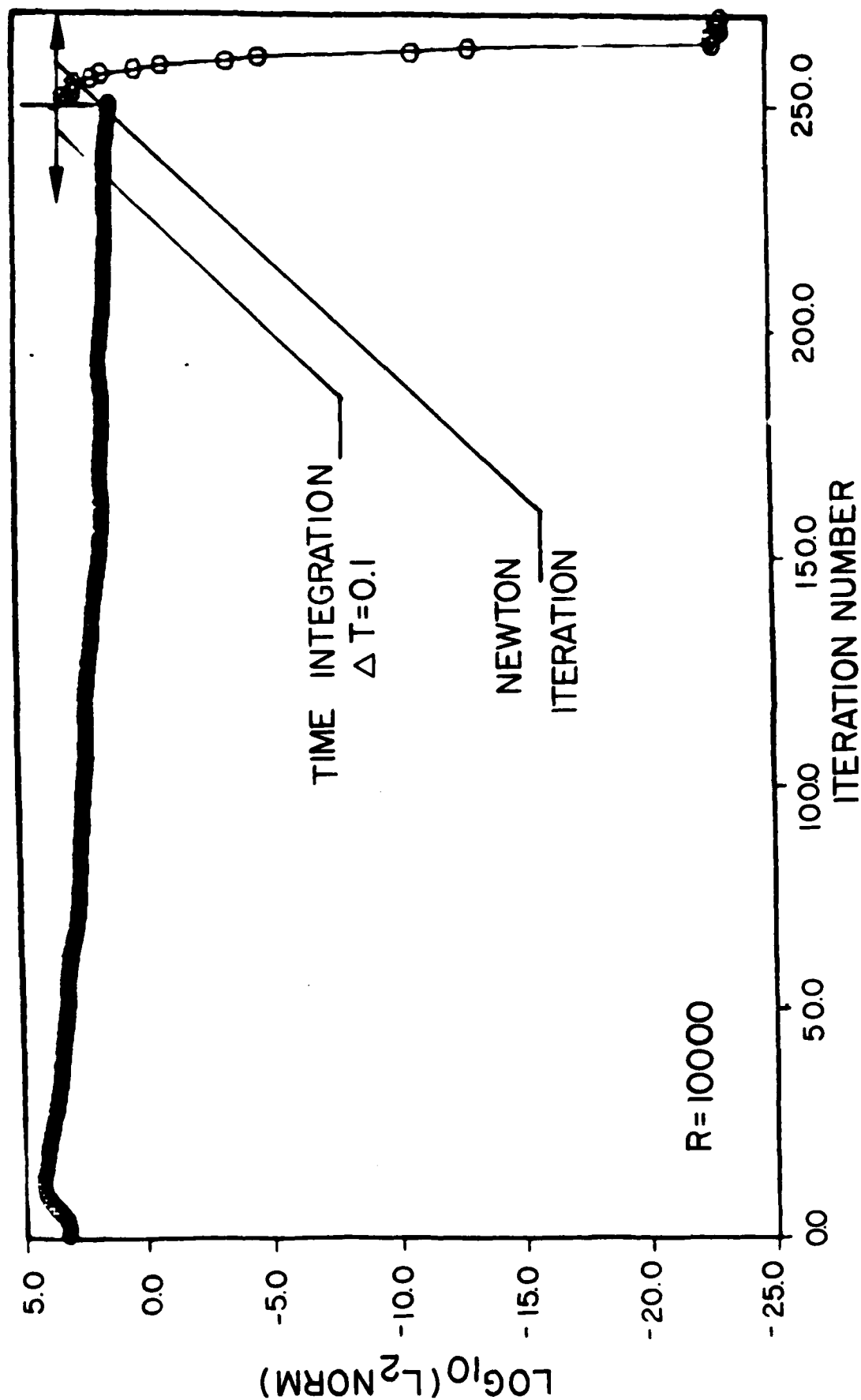


Figure 8. Driven Cavity Convergence History for $R = 10,000$

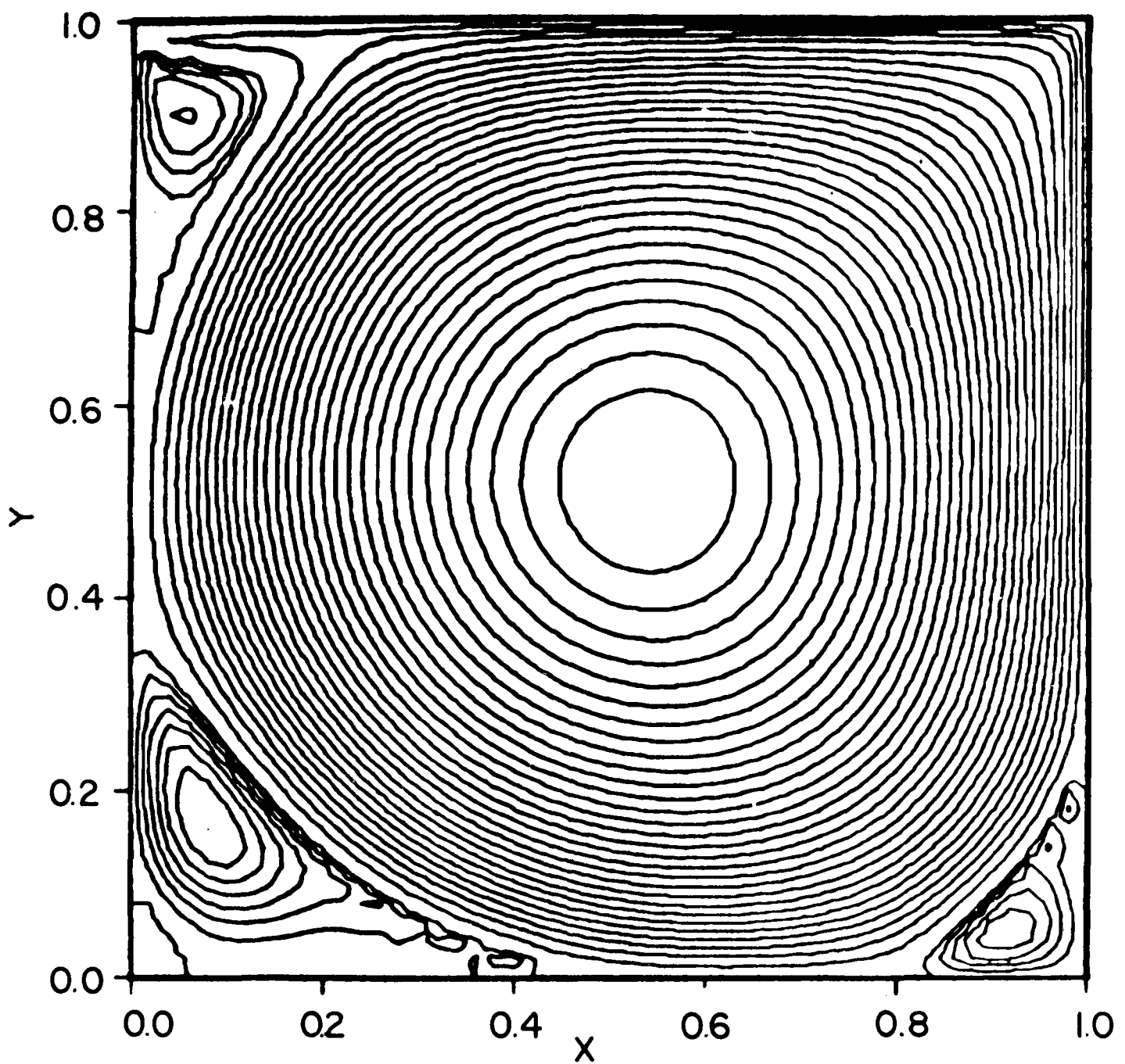


Figure 9. Driven Cavity Streamfunction Contours for $R = 10,000$

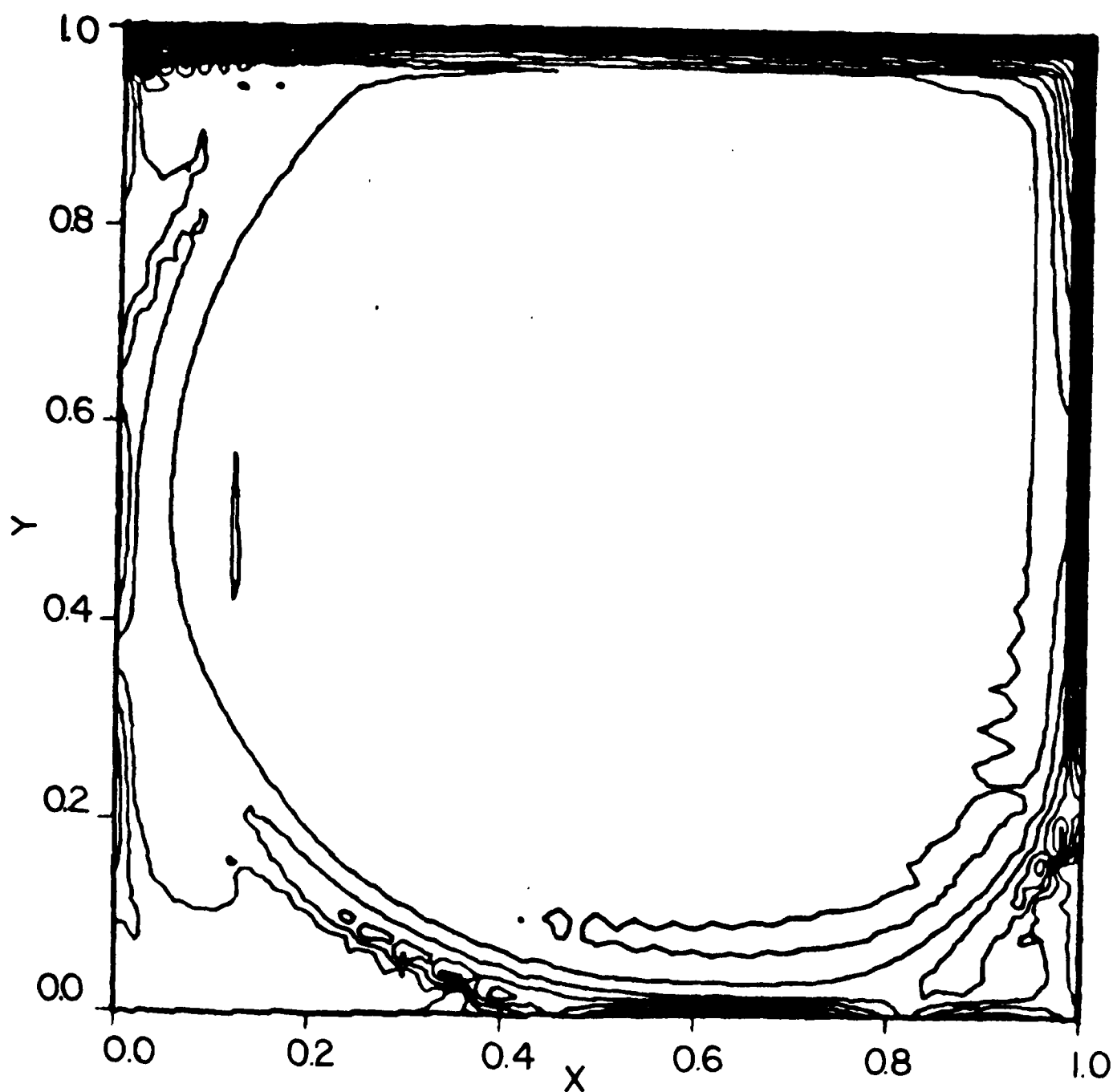


Figure 10. Driven Cavity Vorticity Contours for $R = 10,000$

along the upper and right-hand walls while the center of the cavity is dominated by an essentially constant vorticity. While the physical behavior described here is in qualitative agreement with previous calculations [8], the (51×51) computational grid used for this high Reynolds number flow is inadequate to resolve details with much acuity.

Comparisons of the present results for all three Reynolds numbers with the accurate solutions of Ghia, Ghia, and Shin [8] are displayed in Fig. 11 in terms of velocity profiles through the center of the cavity. The solutions of Ghia et al employed uniform grids of (129×129) for $R = 100$ and $R = 1,000$, and a grid of (257×257) for the $R = 10,000$ solution. As the Reynolds number increases, the formation of strong shear layers along the upper and lower walls is apparent. Agreement between the results is reasonable for the lower Reynolds number solutions, but for $R = 10,000$ a lack of resolution in the wall boundary layers of the present calculation has resulted in the indicated disparity.

Although no numerical anomalies were encountered for the high Reynolds number case presented here ($R = 10,000$), this result must be regarded as preliminary due to the coarse grid which was employed. Many algorithms meet with difficulties as the mesh size is refined. Based upon the stability of the time accurate technique for linear equations with constant coefficients, and the convergence properties of Newton's method, we believe that spatially accurate solutions can be obtained. Such calculations, however, will be resource intensive due to the large linear system involved.

Circular Cylinder

The flow about a circular cylinder is another classic example that has been computed by a number of researchers [4-6, 10, 13], who have obtained both steady and unsteady solutions. Physically, steady flow fields are not commonly observed for Reynolds numbers above a value of approximately 40. Numerically, however, it is possible to obtain steady symmetric flow for much higher values of R . The reason for this is that numeral freestream boundary conditions and surface geometries may be smooth to machine accuracy. If the differencing scheme is perfectly symmetric (as in the present case), then there is no possibility of asymmetry evolving in the

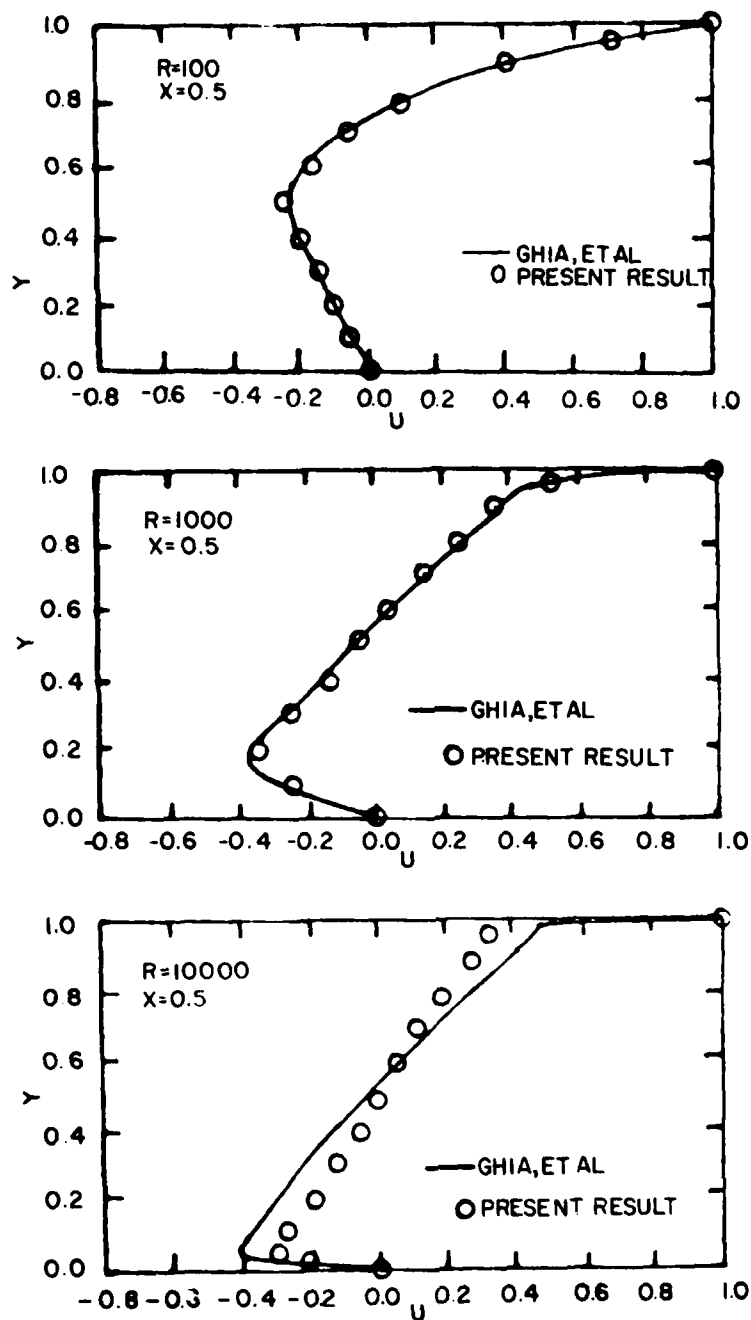


Figure 11. Comparison of Driven Cavity Velocity Profiles with Solution of Ghia, Ghia, and Shin.

solution. Unsteady vortex shedding may be induced, however, by introducing a small perturbation which will eventually form a self-sustained periodic motion for $R > 40$. This technique has been employed in previous calculations [10] and was also incorporated in the results presented here. In the physical situation, there is never perfect symmetry in either freestream conditions or the surface geometry so that the inherently unstable flow will naturally exhibit large scale unsteady motion.

The geometry to be considered consists of a circular cylinder of diameter L immersed in a freestream moving left to right with the reference speed u_∞ at a Reynolds number of 100. The computational O-grid is depicted in Fig. 12 and consists of (121×100) points in (ξ, η) where the ξ -direction is circumferential around the body, the η -direction is normal to it, and the origin is located at the upstream leading edge. A value of $\Delta r = 0.02618$ is employed at the surface and the grid is stretched exponentially to an outer boundary of $r = 100$, r being the radius. Circumferentially, a uniform spacing of $\Delta\theta = 3^\circ$ was employed so that the arc length along the surface was approximately equal to the radial spacing, i.e., $r\Delta\theta \approx \Delta r$. These grid spacings, boundary locations, and number of points are similar to those employed by Jordan and Fromm [10]. The only exception to a constant $\Delta\theta$ occurred at the upstream leading edge where the first and last mesh increments were adjusted so that the ξ -grid line $i = I$ was located between the lines $i = 1$ and $i = 2$ and the line $i = 1$ was located between the lines $i = I-1$ and $i = I$.

The overlapping grid structure at the upstream outer boundary is illustrated in Fig. 13 for clarity. This construction results in ease of application of periodic boundary conditions in the circumferential (ξ) direction. Second-order accurate expressions are obtained by the simple relationships

$$\left. \begin{aligned} \psi_{I,j} &= (\psi_{1,j} + \psi_{2,j})/2 \\ \psi_{1,j} &= (\psi_{I,j} + \psi_{I-1,j})/2 \end{aligned} \right\} 1 \leq j \leq J \quad (45)$$

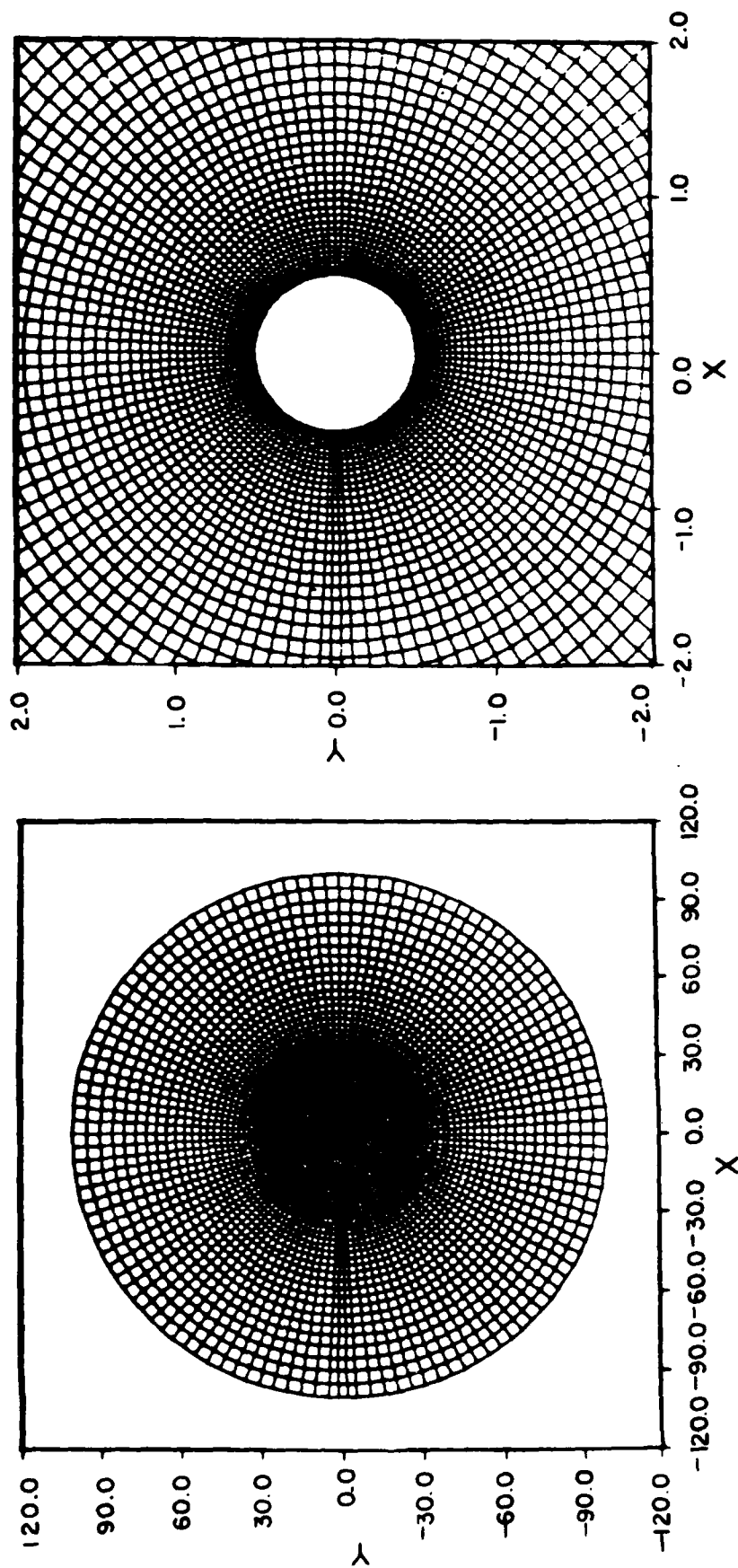


Figure 12. Circular Cylinder Computation Grid

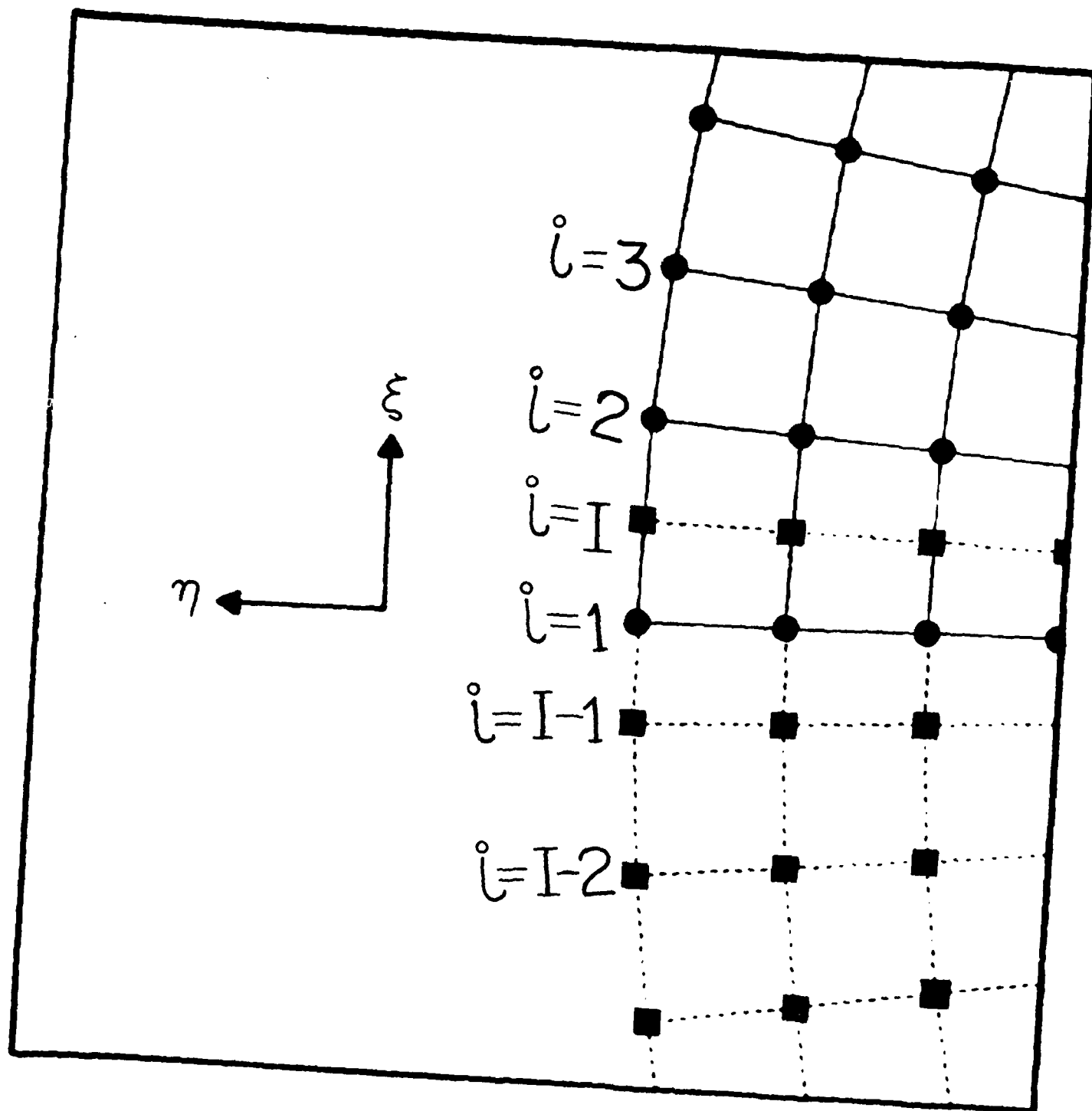


Figure 13. Circular Cylinder Grid Structure at Leading Edge of Computational Domain

with similar representations for ω . These periodic conditions have once again altered the basic structure of the matrix M which now has the form

$$M = \begin{bmatrix} D_1 & E_1 & & & A_1 \\ C_2 & D_2 & E_2 & & \\ & \ddots & \ddots & \ddots & \\ & & C_{I-1} & D_{I-1} & E_{I-1} \\ A_I & & & C_I & D_I \end{bmatrix} \quad (46)$$

Periodic matrices of the type given by Eq (46) are common in numerical problems. Several methods exist for solution of the linear system Eq (20) when M has the form given by Eq (46) [1, 17, 18]. Unfortunately, all such methods require considerable computational effort. We estimated that computing time for solution of the linear system using the periodic form of M represented by Eq (46) would be approximately twice that of the block-tridiagonal system with M given by Eq (22). Furthermore the upstream region of the flow field should not experience any large amplitude unsteadiness. For these reasons, the periodic conditions have been applied explicitly, which of course are only first order accurate in time. Values of ψ and ω were held constant along the ξ -boundaries over a time step or iteration. After all interior points had been calculated at the new level, boundary values were updated according to

$$\left. \begin{aligned} \psi_{1,j} &= (\psi_{2,j} + 2\psi_{I-1,j})/3 \\ \psi_{I,j} &= (2\psi_{2,j} + \psi_{I-1,j})/3 \end{aligned} \right\} 1 \leq j \leq J \quad (47)$$

with similar expressions for ω . Equation (47) follows directly from (45).

Boundary conditions in the η -direction are indicated in Fig 14. On the solid surface, the no-slip conditions were invoked and the reference streamline defined. Along the forward, upper, and lower portions of the outer boundary, freestream conditions prevailed. At the rearward outer boundary, defined by an arc of 72° bisected by the centerline, the conditions $\frac{\partial \psi}{\partial x} = \omega = 0$ were employed. The angle defining the downstream boundary was chosen rather arbitrarily. Other downstream

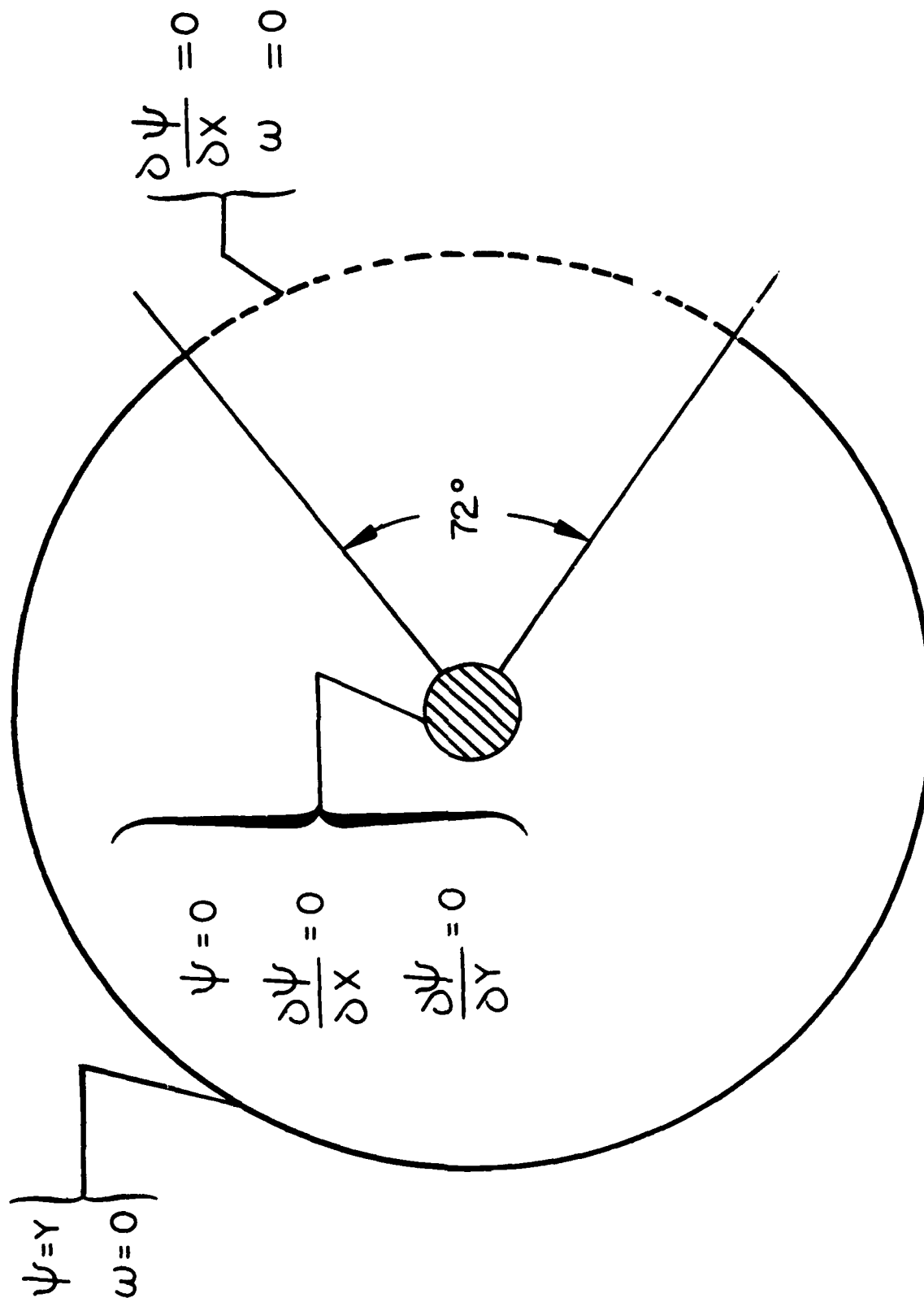


Figure 14. Circular Cylinder Boundary Conditions

conditions were tested, namely $\frac{\partial \psi}{\partial \eta} = 0$ and second-order extrapolation from interior mesh points, and produced no apparent differences in the computed results. We should mention that the condition $\frac{\partial \psi}{\partial x} = 0$ was applied with second-order accuracy. Admittedly the outer boundary conditions are not physically correct. However, the location of this boundary is sufficiently far from the body surface so that such inaccuracy did not contaminate the near field. No numerical difficulties resulted from these conditions, and the appropriateness of their application can be judged a posteriori from the computed results.

For purposes of comparison, we find it useful to generate the pressure distribution about the body surface. This can be obtained from the momentum Eqs (2) and (3) which were transformed to the computational coordinates (ξ, η) . Following the work of Jordan and Fromm [10], we see it is convenient to formulate these equations in terms of total pressure to arrive at

$$\frac{\partial}{\partial \xi} \left[\frac{1}{2} (u^2 + v^2) + P \right] = \frac{1}{J} (\eta_x \frac{\partial v}{\partial t} - \eta_y \frac{\partial u}{\partial t}) + \frac{1}{J} (\eta_x u + \eta_y v) \omega - \frac{1}{R} \left(\frac{\eta_x^2 + \eta_y^2}{J} \right) \frac{\partial \omega}{\partial \eta} \quad (48)$$

$$\frac{\partial}{\partial \eta} \left[\frac{1}{2} (u^2 + v^2) + P \right] = \frac{1}{J} (\xi_y \frac{\partial u}{\partial t} - \xi_x \frac{\partial v}{\partial t}) - \frac{1}{J} (\xi_x u + \xi_y v) \omega + \frac{1}{R} \left(\frac{\xi_x^2 + \xi_y^2}{J} \right) \frac{\partial \omega}{\partial \xi} \quad (49)$$

In deriving (48) and (49), note that continuity and the definition of vorticity have been employed, as well as the orthogonality of ξ and η . At every time step the right-hand sides of (48) and (49) are available so that the η -momentum equation may be integrated from the outer boundary, where $v = P = 0$, and $u = 1$, inward along $y = 0$ to the leading edge. On the solid boundary $u = v = 0$ so that (48) may be integrated from the leading edge in the circumferential direction to obtain the surface pressure distribution. Note that along this path Eq (48) reduces to

$$\frac{\partial P}{\partial \xi} = - \frac{1}{R} \left(\frac{\eta_x^2 + \eta_y^2}{J} \right) \frac{\partial \omega}{\partial \eta} \quad (50)$$

A simple trapezoidal rule was used to perform all integrations. The temporal derivatives appearing in Eq (49) were evaluated using three-point one-sided differences. Having obtained the surface pressure, the lift and drag coefficients were calculated from the following expressions

$$C_L = 2\oint \left[\frac{1}{J} (\eta_y P - \eta_x \omega/R) \right]_{\eta=0} d\xi \quad (51)$$

$$C_D = 2\oint \left[\frac{1}{J} (\eta_x P + \eta_y \omega/R) \right]_{\eta=0} d\xi \quad (52)$$

where the indicated contour integrations around the solid body were computed by trapezoidal rule.

Homogeneous initial conditions were prescribed for the dependent variables at all interior mesh points and the governing equations were integrated in time for 100 steps with $\Delta t = 0.5$. This was followed by 30 steps of Newton iteration which were more than sufficient to obtain a steady symmetric flow field which was converged to machine accuracy. The rate of convergence appeared to be slowed only slightly by the use of explicit periodic boundary conditions. Following the technique employed by Jordan and Fromm [10], unsteady motion was initiated by rotating the cylinder with a tangential velocity equal to 20 percent of the freestream value, first in a clockwise direction for 10 time steps ($\Delta t = 0.5$) and then counterclockwise for 10 time steps. At this point the forced rotation was terminated and integration in time was continued for an additional 100 steps with an increment $\Delta t = 0.5$. This allowed the solution to rapidly evolve to a periodic self-sustained unsteady flow. The time step was then reduced to a value of 0.05 to resolve the temporal content of the solution. Other types of initial perturbation were attempted and all appeared to work equally well. The forced rotation employed here was simply implemented by allowing a nonzero velocity at the cylinder surface.

Time histories of the instantaneous lift and drag coefficients for the calculation appear in Fig. 15 and 16 respectively. Note that the Newton iterations have been indicated by assigning a value of $\Delta t = 0.5$ solely for plotting purposes ($50 \leq t \leq 65$). In the case of steady symmetric flow, Table 1 provides comparison of the present result with several previous calculations in terms of the drag coefficient and pressure coefficient at the forward stagnation point. While the

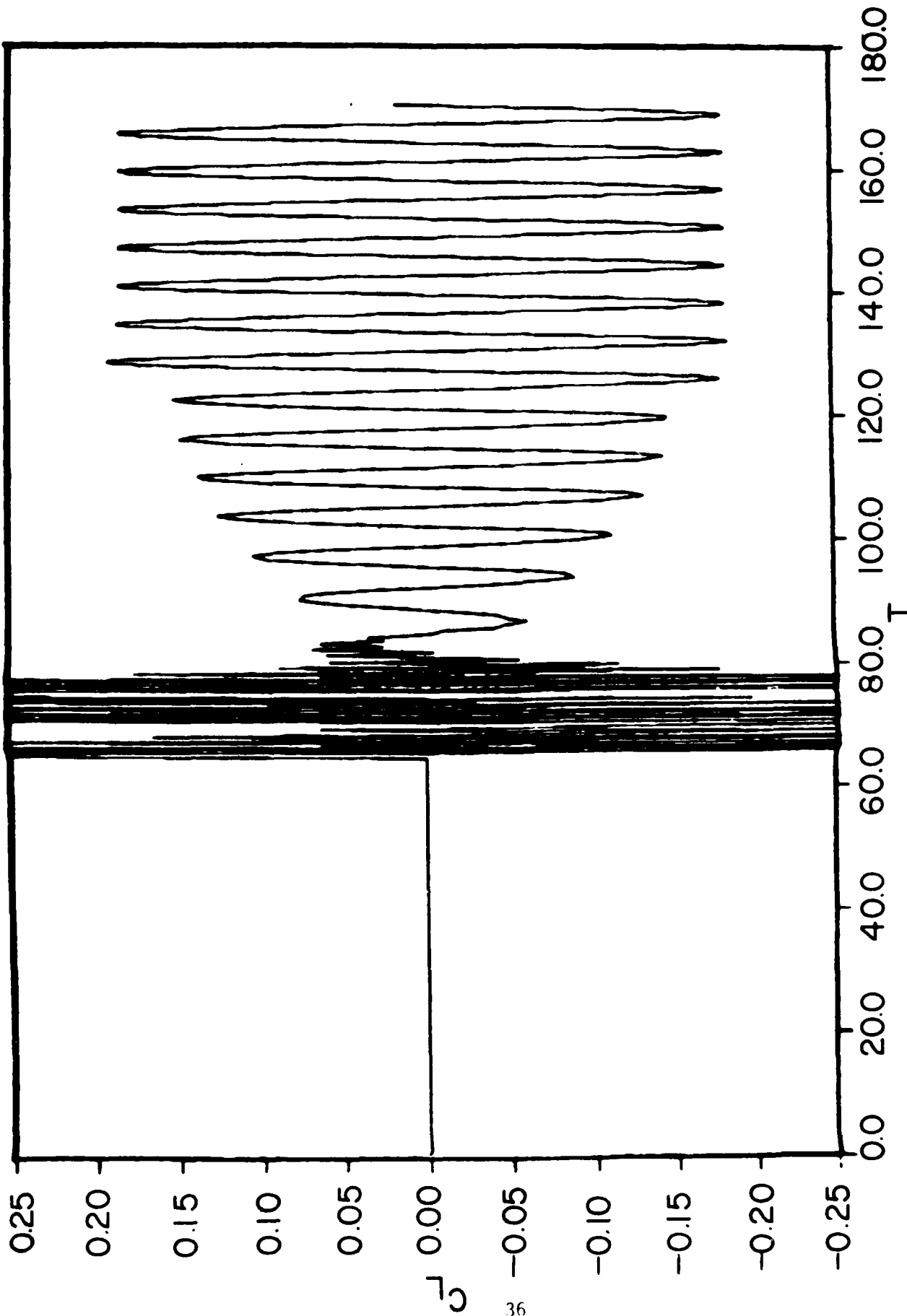


Figure 15. Time History of Lift Coefficient for Circular Cylinder

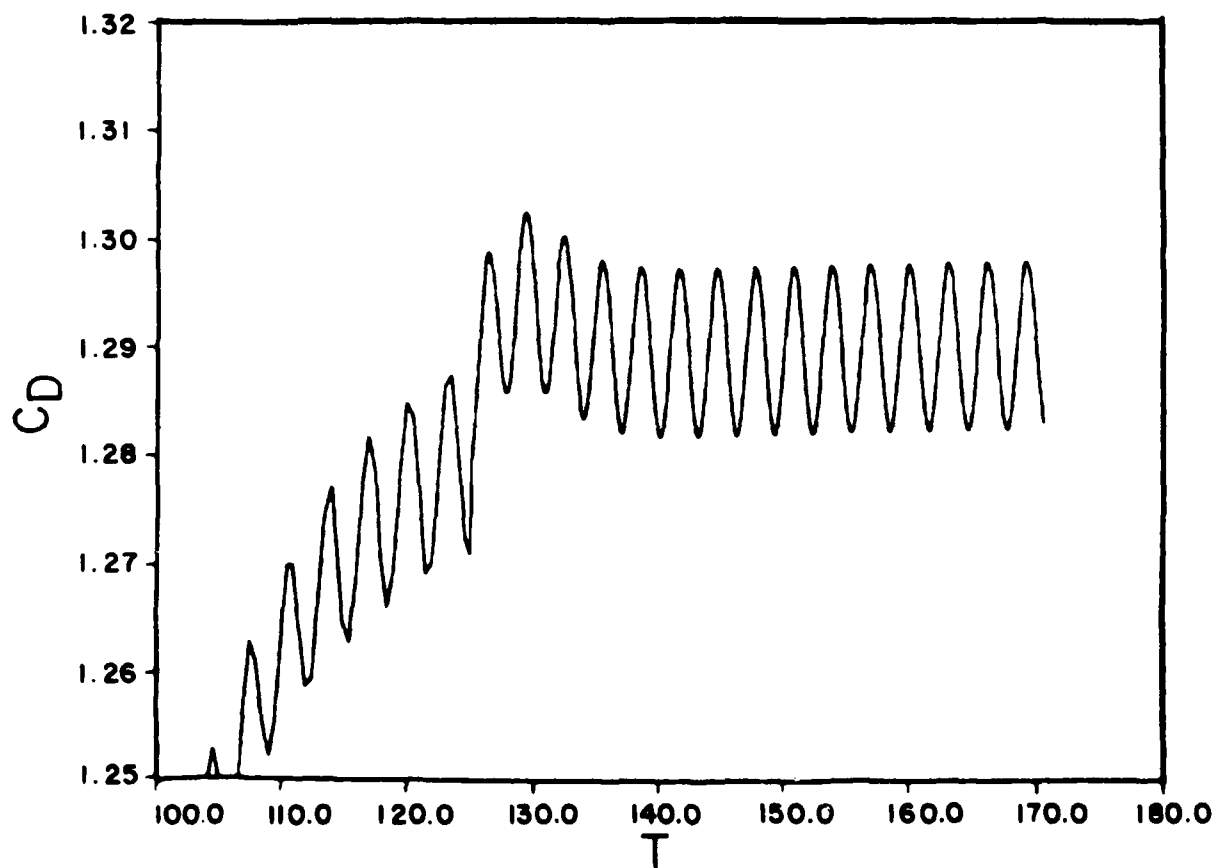
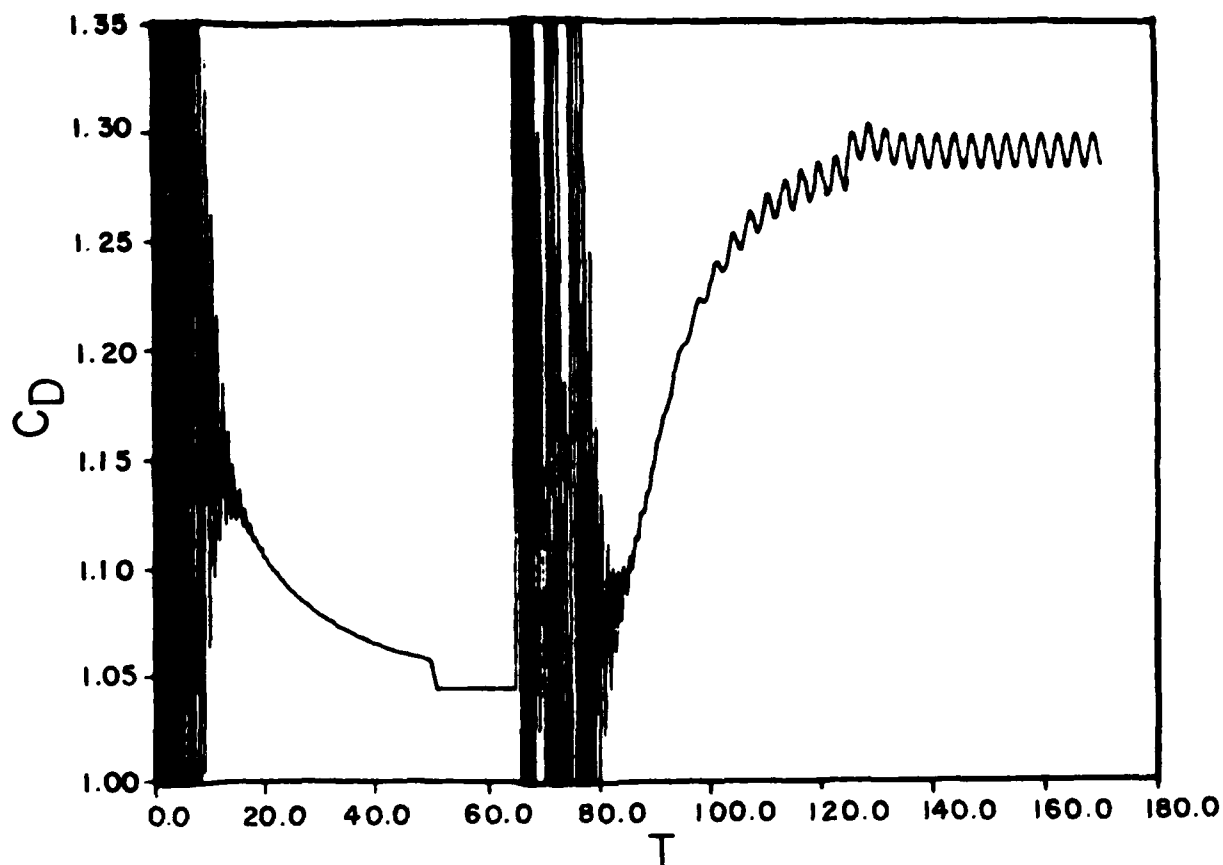


Figure 16. Time History of Drag Coefficient for Circular Cylinder

TABLE 1. Results for Steady Symmetric Flow, $R = 100$

	C_D	Forward Stagnation C_p
Dennis & Chang [4]	1.056	1.060
Jordan & Fromm [10]	1.1	
Fornberg [5, 6]	1.058, 1.060	1.061, 1.065
present result	1.044	1.057

current values are slightly lower than those reported elsewhere, the following observation is significant. After the first 100 time steps the L_2 norm had dropped by approximately eight orders of magnitude. This amount of reduction would usually be sufficient to satisfy most common convergence criteria. At this point the drag coefficient had a value of 1.058, which was appreciably lowered by subsequent Newton iteration (see Fig. 16, $t \approx 50$).

The time histories of the force coefficients indicate that for the unsteady flow which evolved, the solution was quite periodic. Table 2 compares the present calculation with the results of Jordan and Fromm [10] which employed a slightly smaller value of the time increment ($\Delta t = 0.015625$) but had only first-order temporal acuity. Here the mean drag is the average of the maximum and minimum values, the Strouhal number is based upon the period of the lift cycle, and the amplitudes of the force coefficients are peak-to-peak values. The time increment employed in the present computation ($\Delta t = 0.05$) resulted in approximately 120 time steps describing one period of the lift cycle. Differences in the amplitudes of the force coefficients between the two solutions, indicated in Table 2, is attributed to the alternative numerical methods employed in the respective calculations.

TABLE 2. Results for Unsteady Flow, $R = 100$

	mean C_D	Strouhal number	C_L amplitude	C_H amplitude
Jordan & Fromm [10]	1.26	0.16	0.54	0.012
present result	1.290	0.162	0.365	0.015

Figure 17 displays instantaneous streamfunction contours for the unsteady flow field. The values of time indicated in the figure are given in radians and referenced to an origin which corresponds to the beginning of the last lift cycle shown in Fig. 15. Evolution of the vortex shedding is apparent. Antisymmetry between solutions which are π radians apart in time is also evident. Corresponding contours of vorticity appear in Fig. 18. Although the near-body field appears to be adequately resolved, the shed vorticity dissipated in the downstream wake owing to the coarseness of the stretched grid and the homogeneous downstream boundary conditions. Comparison of the mean drag coefficient with the experimental data of Wieselsberger [21] and Tritton [20] is provided in Fig. 19. The present result is seen to fall well within the experimental scatter. In Fig. 20 the Strouhal number is compared to the measurements of Roshko [16]. We see that the comparison is adequate despite the fact that the current value may be considered slightly low.

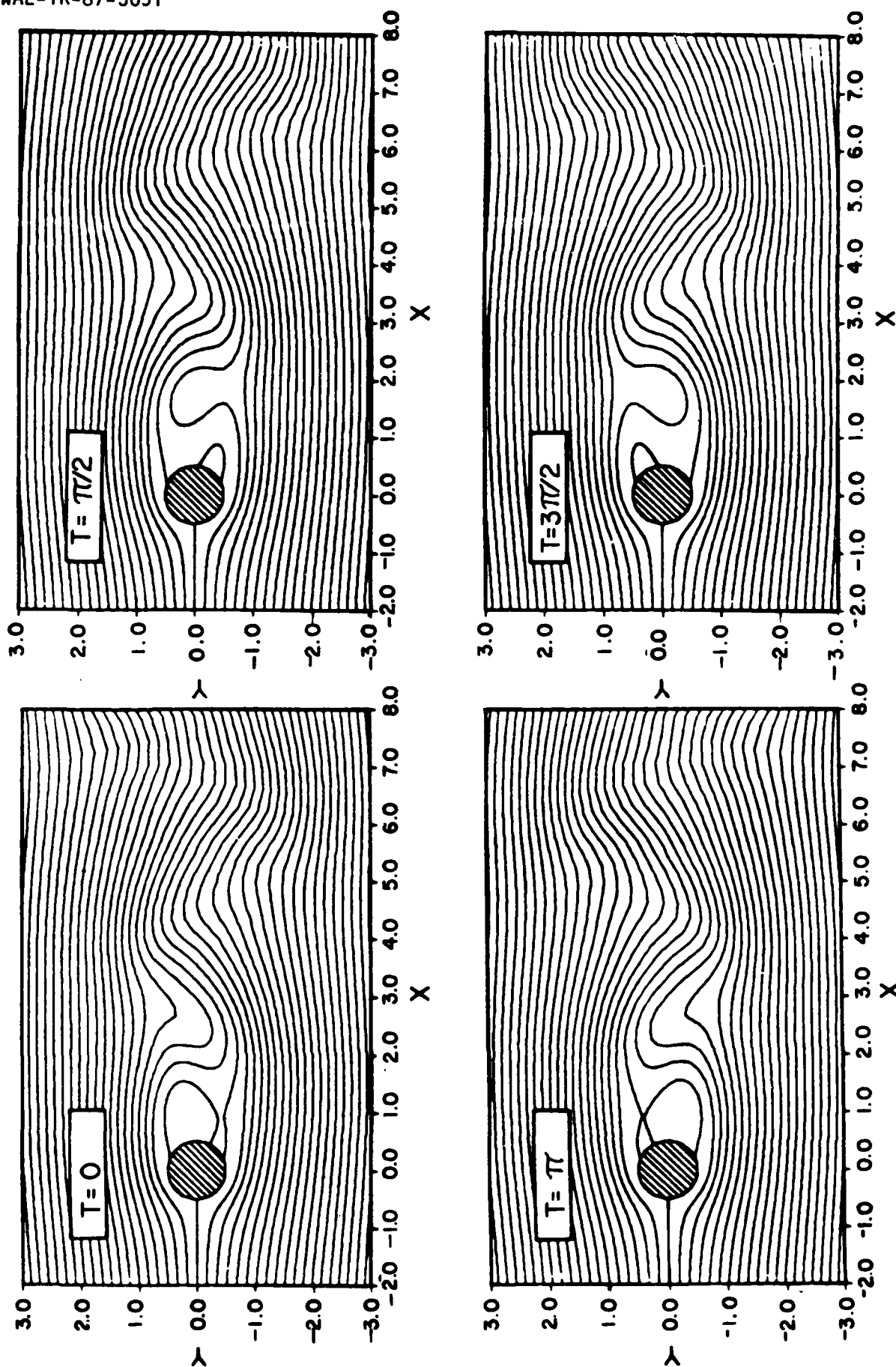


Figure 17. Instantaneous Streamfunction Contours for Circular Cylinder

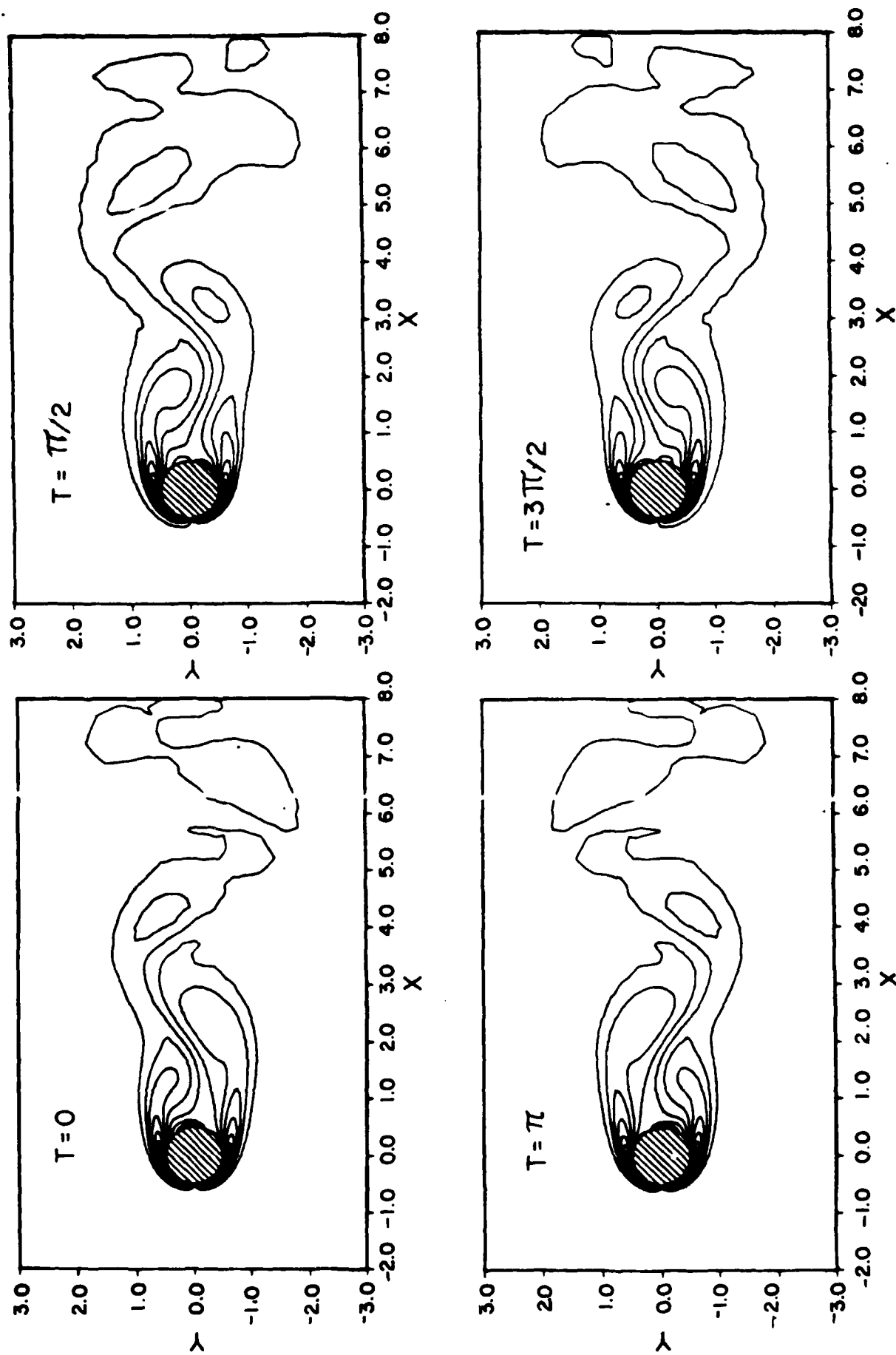


Figure 18. Instantaneous Vorticity Contours for Circular Cylinder

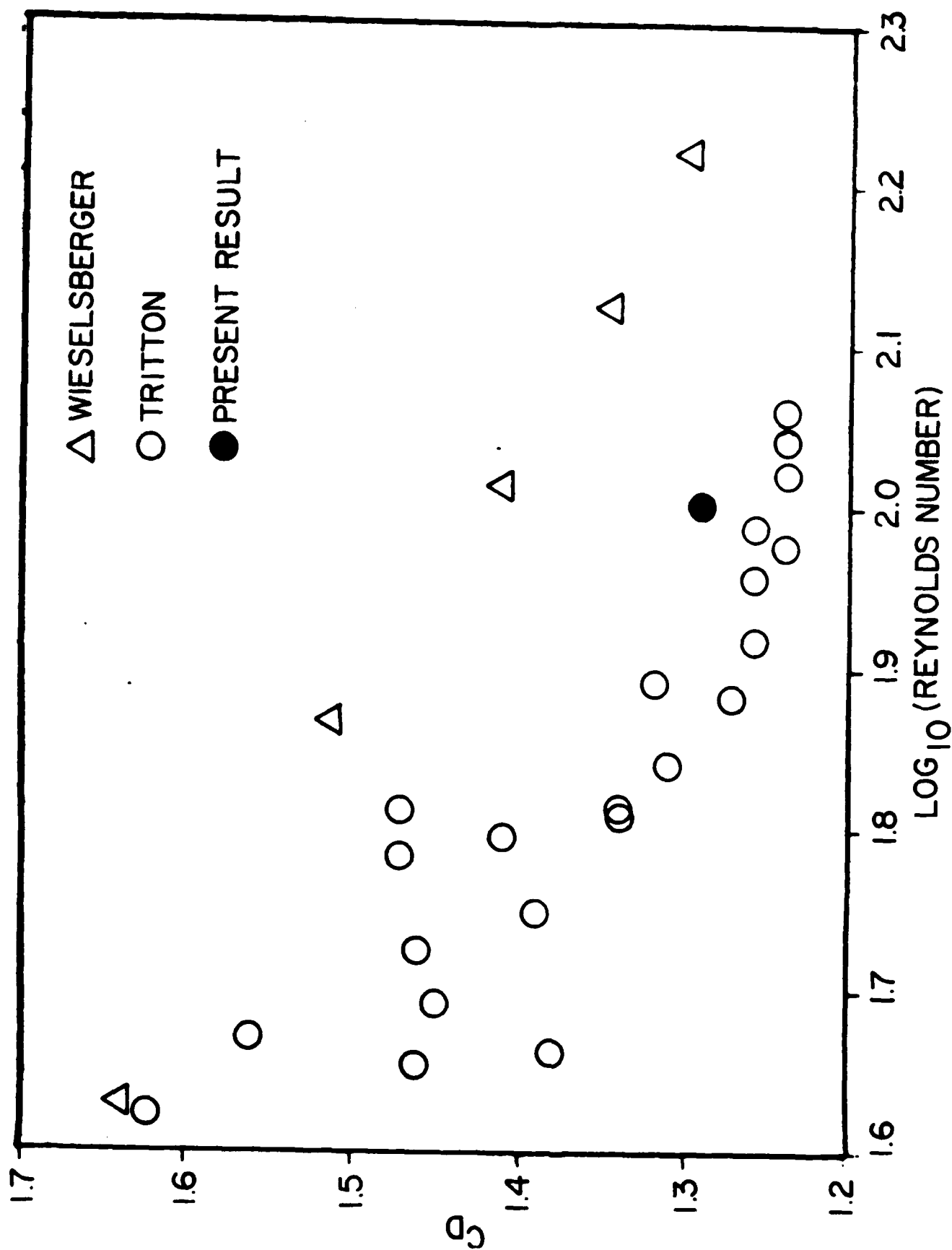


Figure 19. Comparison of Drag Coefficient for Circular Cylinder with Experiment

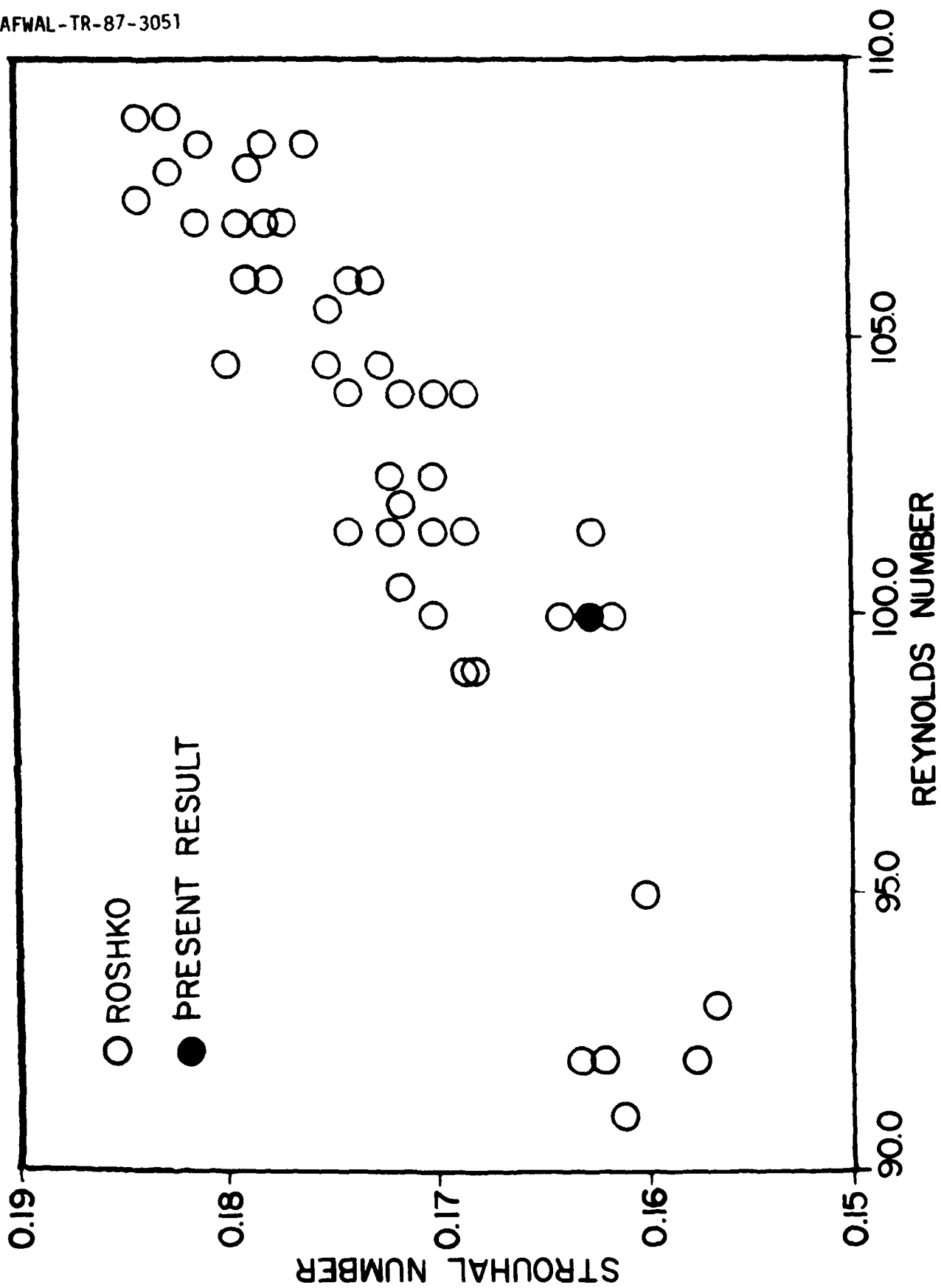


Figure 20. Comparison of Strouhal Number for Circular Cylinder with Experiment

SECTION VI

DISCUSSION

The numerical method presented here affords a simple and straight-forward approach for obtaining both steady and unsteady solutions to the Navier-Stokes equations. In fact, it is only the previous limitations of computing capacity which have precluded its prior implementation. The unified formulation provides a means of calculating time accurate solutions or of arriving at an initial iterate so that steady results may be achieved via Newton's method. Without this feature, Newton iteration may not be useful for general applications as there exists no practical technique for generating initial solutions which will converge. Note that the method is applicable to other sets of equations, especially those in conservation law form, as for example the compressible Navier-Stokes equations.

While the algorithm does possess certain attractive features, its use requires extensive computer resources. The ultimate efficiency of the method is determined by the solution technique employed for the linear system. In this regard, the block-Gaussian method used here is not considered to be optimal in terms of either computational time or storage. We selected it because of ease of implementation and it is not central to the numerical algorithm. Additionally, it maintains certain advantages over other solving procedures. Because the block matrices are considered dense, no special logic is required to satisfy the wall compatibility relationship for vorticity in the n -direction. Although these matrices are initially sparse, the storage they provide is utilized in the solution process. All of the results presented here were generated on a CRAY XMP-12 computing system. For the (51×51) grid employed for the driven cavity problem approximately 1.85-million decimal words of central memory were required and a data processing rate of 1.0×10^{-3} central processing unit (CPU) second/time step/grid point was achieved. Total computation time to attain machine accuracy for each of the cavity solutions is provided in Table 3.

TABLE 3. Computational Time for Driven Cavity

	R = 100	R = 1,000	R = 10,000
CPU second	20.8	148.3	686.9

One final advantage of the block-elimination method is the fact that external storage devices easily may be employed rather than central memory. Because only a few of the blocks need reside in core at one time, they may be defined, modified, stored sequentially, and later accessed sequentially as needed. This technique was utilized for the cylinder calculation, at the expense of additional I/O time. For the (121 x 100) grid employed for this computation, only 0.58-million decimal words of central memory were required because of the use of external storage. A data processing rate of 8.1×10^3 CPU second/time step/grid point was attained, resulting in a total computational time of 31.7 CPU hours for the unsteady cylinder flow. We reemphasized that the cited processing rates could be considerably reduced by making use of a more efficient solving technique than the block-elimination procedure employed here.

REFERENCES

1. J. H. Ahlberg, E. N. Nilson, and J. L. Walsh, The Theory of Splines and Their Applications (Academic Press, New York/London, 1967), p. 15.
2. R. M. Beam and R. F. Warming, AIAA J. 16, 393, (1978).
3. O. R. Burggraf, J. Fluid Mech. 24, 113 (1966).
4. S. C. R. Dennis and G.-Z. Chang, J. Fluid Mech. 42, 471 (1970).
5. B. Fornberg, J. Fluid Mech. 98, 819 (1980).
6. B. Fornberg, J. Comput. Phys. 61, 297 (1985).
7. J. E. Fromm and F. H. Harlow, Phys. Fluids 6, 975 (1963).
8. U. Ghia, K. N. Ghia, and C. T. Shin, J. Comput. Phys. 48, 387 (1982).
9. E. Isaacson and H. B. Keller, Analysis of Numerical Methods (John Wiley & Sons, New York/London/Sydney, 1966), p. 115.
10. S. K. Jordan and J. E. Fromm, Phys. Fluids 15, 371 (1972).
11. H. B. Keller and T. Cebeci, AIAA J. 10, 1193 (1972).
12. U. B. Mehta and Z. Lavan, J. Fluid Mech. 67, 227 (1975).
13. F. Nieuwstadt and H. B. Keller, Comput. Fluids 1, 59 (1973).
14. G. A. Osswald, K. N. Ghia, and U. Ghia, "Study of Incompressible Separated Flow Using an Implicit Time-Dependent Technique," AIAA Paper No. 83-1894, 1983.
15. P. J. Roache and T. J. Mueller, AIAA J. 8, 530 (1970).
16. A. Roshko, "On the Development of Turbulent Wakes from Vortex Streets," NACA TN 2913, 1953.
17. J. S. Steger, "Implicit Finite Difference Simulation of Flow About Arbitrary Geometries with Application to Airfoils," AIAA Paper No. 77-665, 1977.
18. C. Temperton, J. Comput. Phys. 19, 317 (1975).
19. A. Thom, Proc. R. Soc. London, Ser. A 141, 651 (1933).
20. D. J. Tritton, J. Fluid Mech. 6, 547 (1959).
21. C. Wieselberger, Phys. Z. 22, 321 (1921).